Using Single Station Seismology to Determine the Structure Beneath the Ross Ice Shelf, Antarctica

Siobhan Light

April 25, 2023

Advisor: Nicholas Schmerr

GEOL 394

Table of Contents

Abstract

Icy ocean worlds, including the moons Enceladus, Europa, and Titan, have a strong potential for astrobiology, making these worlds the subject of upcoming and proposed exploration missions. To determine if these moons are habitable, knowledge of their physical internal structure must be established to determine where suitable habitats might exist. Geophysical approaches such as collection of seismic energy generated on these tidally active worlds via a landed seismometer would lend valuable insight into their physical characteristics. However, there remains a pressing scientific need to develop methodology capable of determining ice shell thickness based on the data from a single seismometer. This study uses the Ross Ice Shelf in Antarctica as a terrestrial seismic analog to investigate how such an instrument could be used to determine the subsurface structure of icy ocean worlds icy ocean worlds. These results can test the hypothesis of whether there is a gradual or sharp transition occurs at ice-ocean interface, an important piece of structural knowledge that would inform models of both ice shelves and ocean world ice shells. Data was continuously collected over a period of 25 months from 2014 to 2016 by a single three-component broadband seismometer located near the WR4 rift of the Ross Ice Shelf, a region that shares multiple physical similarities to the Tiger Stripe Fractures region of Enceladus. To test this hypothesis, over 650 seismic events had P-wave and Rayleigh-waves identified among initial inspection. On average, these events occurred 2.7 ± 0.4 kilometers from the seismometer. Inspection of the moveout of the highest-quality seismic signals found that individual icequakes were sufficient to use to determine seismic structure. To improve the accuracy of identified picks, 65 of the highest-quality signals had their P-wave and Rayleigh-waves identified more accurately via frequency-dependent polarization analysis. Velocity spectral analysis of those events found that seismic wave arrivals in the data match those predicted by a velocity model for a sharp ice-shelf structure of 300 meters and ocean depth of 700 meters. Further events would need to be analyzed in order to support the alternative hypothesis of variation in the structure of the ice shelf at the ice-ocean interface. Nevertheless, this study shows how single-station seismology can resolve underlying structure in cryosphere settings.

Plain Language Summary

On Earth, we learn about the underlying structure of our planet by analyzing the data contained in earthquake signals. In our solar system, icy ocean worlds are planets suspected or known to have a liquid ocean under a solid layer of ice acting as a shell around it. These worlds likely experience icequakes in part as a consequence to the same processes that lead to these worlds having an interior ocean. Since icy ocean worlds are prime candidates for life beyond Earth, scientists are interested in exploring these moons in future space missions. However, we would need to develop new methods to analyze icequake data from icy ocean moons since we have never had such a mission occur before. Furthermore, scientists would be very interested to understand what is occurring where the ice shell transitions to an ocean since whether this is a sharp boundary or "mushy" would have important implications for any potential life. Since it would be difficult to develop such a methodology on an icy ocean world since they are far away, it is much easier to do that on Earth were large ice shelves overly oceans. Many questions remain about Earth's ice shelves so their structure is also important to scientists. In this study, we looked at icequakes that occurred near a rift on Earth's largest ice shelf, the Ross Ice Shelf. In particular, we looked only at the data recorded by a single seismometer since that is the likely setup for a mission to an icy ocean world. The types of waves contained in an icequake were first manually identified in order to determine how far away the icequakes occurred from the seismometer. Some of these picks were then refined by a more sophisticated analysis designed to separate signals with different characteristics. Not many events were reanalyzed with this more sophisticated method, but a basic structure of the iceshelf could be matched with the data. As a result, this study shows that a single seismometer would be sufficient to learn about the basic properties of an icy ocean world's shell, but further analysis would need to be done to see if it is possible to find variation in the ice shelf structure with just the data collected by a single seismometer.

Introduction

Icy ocean worlds are places in our solar system suspected or known to harbor a liquid ocean beneath a solid ice layer. Several of these worlds, including Europa, Titan, and Enceladus, are considered promising environments to harbor life beyond Earth (Hendrix et al., 2019). To assess whether an icy ocean world is potentially habitable, knowledge of the physical and chemical characteristics of these planets is crucial (Hendrix et al., 2019; Marusiak et al., 2021). For example, the physical properties of their external ice shells and outer surfaces would influence their habitability (Hand et al., 2009) and extent to which biosignatures may be expressed on their surfaces (Figueredo et al., 2003). As a result, planetary scientists are currently interested in understanding the physical characteristics of these icy shells, including their thickness, composition, porosity, rheology, and the spatial and temporal variations in these properties (Hendrix et al., 2019). Future geophysical investigations to address these questions is crucial to the exploration of icy ocean worlds (Marusiak et al., 2021). Seismometers are a critical tool in a geophysics toolkit, and as pointed out in Vance et al. (2018), there is a need to develop techniques to analyze the data these seismometers would collect. Upcoming and proposed missions to icy ocean worlds magnify this need. For instance, seismic exploration of Titan intending to infer the interior structure of this moon will occur via a geophone instrument included on the upcoming Dragonfly mission (Lorenz et al., 2018). Furthermore, the recent Planetary Science Decadal Survey for 2023-2032, the document outlining the scientific priorities of the planetary science community for the next decade, stated that a top priority is to send a lander mission with geophysical instrumentation to Enceladus (National Academies of Sciences, Engineering, and Medicine, 2022). Recent research has highlighted that radar sounding alone is unlikely to detect the ice-ocean interface of Enceladus due to radar attenuation within its shell (Souček et al., 2023).

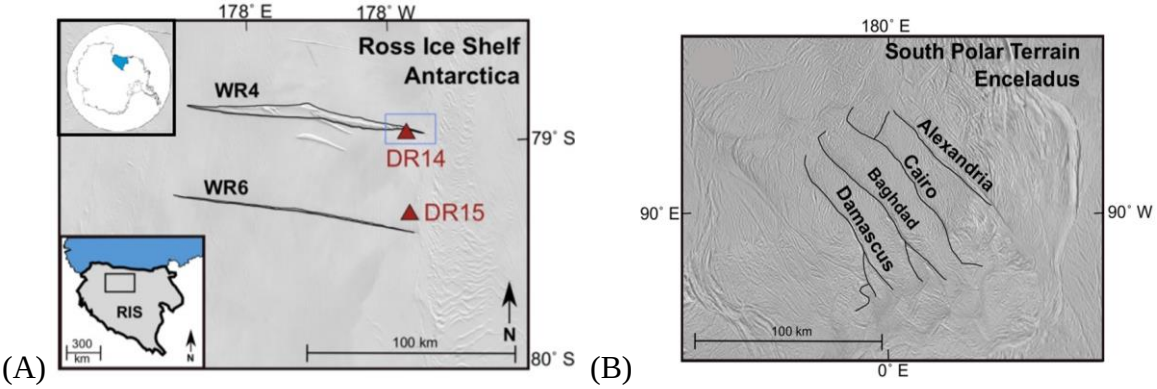

Figure 1: Part of Figure 1 from Olsen et al. (2021). Both maps have the same scale. (A) Map showing the location of the study area, including the location of the Ross Ice Shelf within Antarctica and the specific area of interest to this study within the Ross Ice Shelf. This study utilized data collected by seismic station DR14 (red triangle symbol inside blue rectangle) located ~2 kilometers south of the WR4 rift. (B) Map of the Tiger Strip Fractures on Enceladus.

Consequently, another methodology is needed to determine the thickness of an icy structure based on the data a single seismometer may collect. One potential approach to develop such a methodology is to see whether an equivalent technique could be developed here on Earth where in situ data can be more readily gathered. Terrestrial ice seismic investigations have approached questions similar to those asked about icy ocean worlds (Podolskiy and Walter 2016) such as determination of subsurface structure (e.g. Zhan et al., 2013). In Antarctica, the Ross Ice Shelf is the world's largest ice shelf, and it has numerous characteristics that arguably make it the closest terrestrial analog to the shells of icy ocean worlds (Olsen et al., 2021). The Ross Ice Shelf is generally in hydrostatic equilibrium with the ocean and its interior is isolated from potentially different forces including tidally driven hinging deformation, short-period ocean perturbations, and ice front microseismicity (Olsen et al., 2021; Brunt et al., 2010; Aster et al., 2021).

The South Pole Terrain of Enceladus, which included the Tiger Strip Fractures, is a tectonically active region of this Saturnian moon where the ice shell may only be a few kilometers thick as opposed to other regions of the moon where the ice shell is tens of kilometers thick (Rhoden et al., 2020; Marusiak et al., 2021). As such, the thinner structure more readily allows comparison to the relatively less thick terrestrial counterpart (with the Ross Ice Shelf ~1 kilometer thick at most) (Das et al., 2020). In this study, I chose to focus on the West Ross rift 4 (WR4) (Walker et al., 2013) which shares several important physical similarities to the Tiger Strip Fractures (Olsen et al., 2021). These similarities include:

1) Comparable geometries (see Figure 1), including lengths, widths, and inter-rift spacing. For example, the Tiger Stripe Fractures are ~115 kilometers in length (Olsen et al., 2021; Crow-Willard and Pappalardo 2015) while WR4 is ~120 kilometers in length (Olsen et al., 2021).
2) Both regions being concentrated regions of deformation. Although the entire Ross Ice Shelf is subject to tidal flexure, the location of WR4 was found by geodetic and seismic evidence in Olsen et al. (2021) to be considered a location of concentrated deformation. Similarly, although the entire South Pole Terrain of Enceladus is subject to tidal flexure, heat flux observations determined a similar conclusion regarding the Tiger Stripe Fractures (Porco et al., 2014).
3) Daily cycles of tidal deformation on similar time scales (~24 hours on Earth compared to ~33 hours on Enceladus) (Olsen et al., 2021).
4) General mechanics regulating ice fracture are not expected to differ between Enceladus and Earth (Olsen et al., 2021).
5) Despite differences in temperature, the generation of seismicity should be comparable between the two objects due to similar coefficients of kinetic friction (Olsen et al., 2021). Even considering their respective temperatures, their coefficients of kinetic friction are similar between the Tiger Strip Fracture region and the Ross Ice Shelf, which is important given that this parameter determines the amount of shear stress needed to

maintain sliding along existing fractures. This informs seismicity since in the warmer Antarctica ice, sliding blocks of ice have strike-slip motion, and laboratory experiments of ice at Enceladean surface temperatures have found the same motion occurs (Schulson and Fortt 2012; Olsen et al., 2021). Another consequence is that the relationship between tidal stress and seismicity is expected to be similar between the two bodies.

Using seismic information gathered by the same seismic station that is the subject of this study (DR14), Olsen et al. (2021) was able to make predictions of seismic activity along the Tiger Stripe Fractures. For example, high signal-to-noise icequakes at least as small as those observed on the Ross Ice Shelf were predicted to be detected by a single seismometer located within several kilometers of the Tiger Stripe Fractures. Although the study focused on rifts on Enceladus, the physical relationships examined involving stress and seismic activity is expected to be applicable to other icy worlds, demonstrating how the region in this study has precedent being a seismic analog for icy ocean worlds.

There are also open questions regarding the structure of terrestrial ice shelves, such as the nature of the ice-ocean interface. For ocean worlds, processes that likely occur at their ice-ocean interface such as accretion when ocean water freezes to form ice are predicted to affect their ice shell's bulk properties (Buffo et al., 2020; Wolfenbarger et al., 2022). Wolfenbarger et al. (2022) studied two classes of accreted ice on Earth found at the base of ice shelves, frazil ice and congelation ice, as an analog to predict the possible nature of accreted ice on icy ocean worlds (Wolfenbarger et al., 2022). Frazil ice forms within a supercooled water column via crystallization and it tends to have a granular texture, while congelation ice forms when water freezes at a solid ice interface and tends to have a columnar texture. The type of accreted ice and the conditions that lead to their formation affects whether the ice-ocean interface is cellular or planar in morphology, and the type of morphology affects the degree to which impurities may become incorporated in the ice. In the natural world, accreted ice is rarely exclusively frazil or congelation ice. The study in part reviewed an ice core previously taken of the Ross Ice Shelf (as well as other ice cores) that was composed of congelation ice, but core taken near rifts on other ice shelves were in part frazil ice. However, more work is needed to understand the nature of accreted ice at the terrestrial ice-ocean interface, including specifically by rifts. Theoretical models suggest the existence of stable "mushy layers" where ocean worlds ice shells are thickening and terrestrial analogs can play an important role in testing such models (Buffo et al., 2021). Some properties of the ice-ocean interface including thermal gradients, basal temperatures, and pressures below places like the Ross Ice Shelf are expected to be of a similar order to that below Europa's ice shell (Lawrence et al., 2023).

Limited seismic investigations have been previously performed looking at this question. King (1994) describes the results of an analysis of seismic reflection data taken across a rift on the northwest Ronne Ice Shelf and found that the rift had an asymmetrical base with differences in the dip of the ice-ocean interface in different areas of the rift accompanied by differences in acoustic impedance.

The processes underlying rifting are also important to understand since it is the precursory process to iceberg calving, which is a critical process to the Antarctic ice sheet's mass balance with implications for ice shelf stability and global sea levels (Walker et al., 2013). Watkins et al. (2021) examined ground-penetrating radar data of the topography of multiple Antarctic ice shelves, including the Ross Ice Shelf, and found that rifts increased the observed roughness (topographic variations in ice thickness). However, current ice shelf models predict smoother topography than their observations indicated. They also suggest that increased roughness is strongly correlated with higher basalt melt rates but there is a need to understand meter-scale features so ice shelf models can be improved and discern the complex interactions between the ocean and ice shelves. Stevens et al. (2020) took a borehole from the central region of the Ross Ice Shelf that found ephemeral refreezing on the ice shelf base similarly suggesting the complex nature and processes that may be occurring in this region. There are also planetary analog implications since planetary tidal stress on some ocean worlds likely causes surface fracturing and faulting (Grebmeier 2022).

The ROSETTA-Ice airborne survey (Tinto et al., 2019) employed ice penetrating radar during a three-year study (2015-2017) of the Ross Ice Shelf to better understand basal melting beneath the Ross Ice Shelf (Das et al., 2020). Figure 2 shows an image derived from the Deep ICE Radar (DICE) dataset of a perpendicular cross-section of the DR14 rift (located around 79.1° S), with a dashed line specifically highlighting the location of the ice-ocean interface. This data suggests complex structure in the ice-ocean interface in proximity to this Ross Ice Shelf rift.

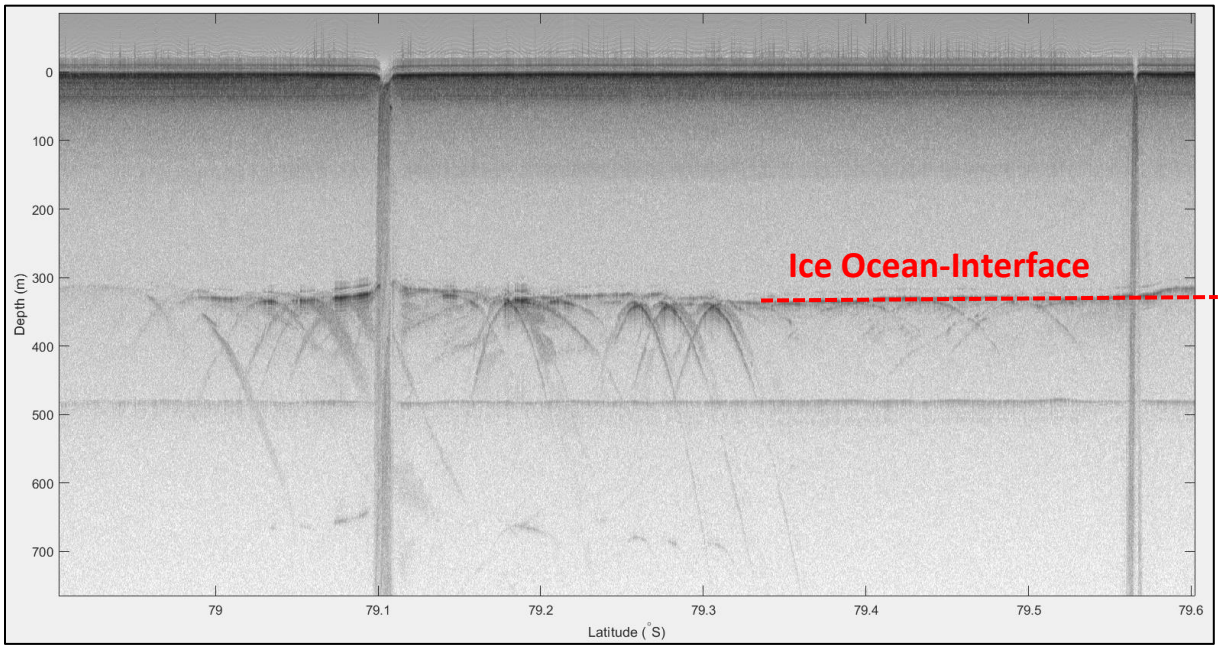

Figure 2: Image of a perpendicular cross-section of the DR14 rift (~79.1° S) taken with the ROSETTA-Ice campaign's Deep ICE (DICE) radar instrument where a red dashed line indicates the location of the ice-ocean interface.

Hypothesis

This study will analyze the waveforms of multiple icequakes recorded by a single seismometer located on an interior rift of the Ross Ice Shelf (the DR14 rift) in order to identify distinguishable reflections off the water-ice interface. An example of such a wave would be the "PvP ice" vector shown in Figure 3. If there are distinguishable reflections, they enable the characterization of the general morphology of the ice shelf (e.g., its overall thickness). Estimations can be made about several physical characteristics of the ice shelf including its thickness, attenuation, and reflection coefficient at the water-ice interface. The null hypothesis of this project is that these reflections will reveal a sharp transition from the ice shelf to the ocean that imply a flat structure and limited ice-ocean interaction. However, the alternate hypothesis is that reflections off the ice-ocean interface will reveal a gradual material transition from the ice shelf to the ocean. This could imply a "mushy layer" structure. It also may be possible that there may be no distinguishable reflections if attenuation in the ice shelf or other noise characteristics of the data makes such reflections too difficult to detect.

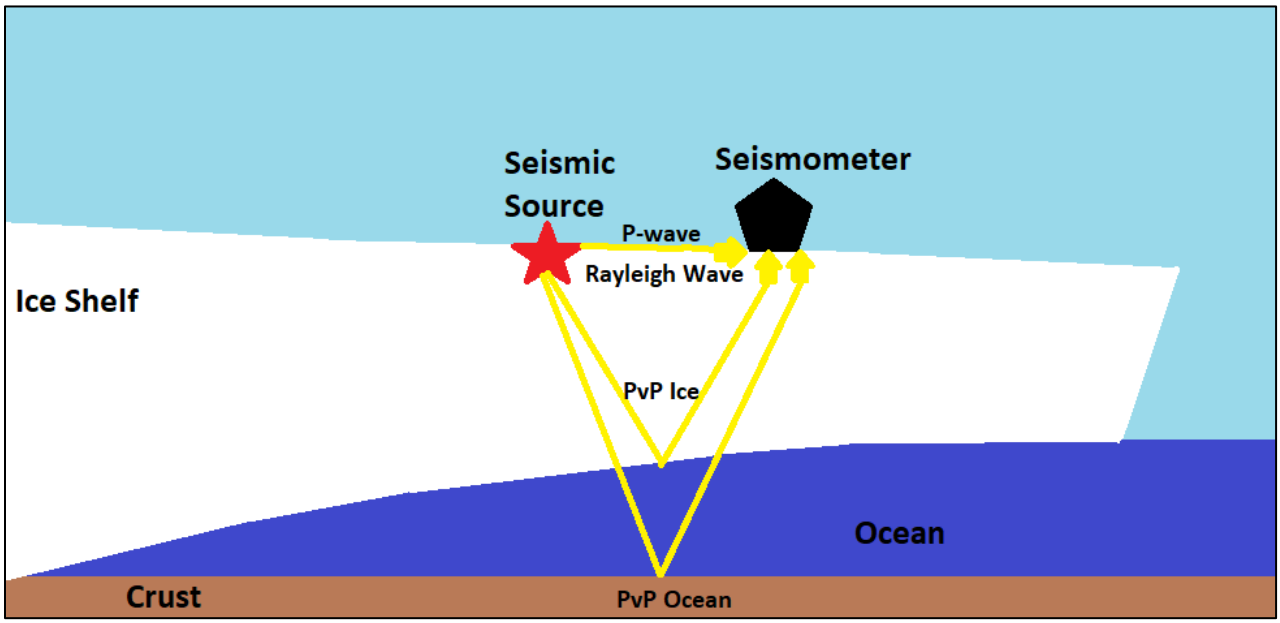

Figure 3: Sketch of an ice shelf overlying an ocean and oceanic crust. A seismic event originating at the location of the red star sends various waves of energy (in the form of yellow vectors) that are received by a seismometer located at the black pentagon. The paths of direct P- and Rayleigh-waves, a P-wave bouncing off the bottom of the ice shelf, and a P-wave that bounces off the bottom of the ocean are shown.

Data

From November 2014 to November 2016, 34 three-component broadband seismic stations in the DRIS seismographic network were fully deployed on the Ross Ice Shelf (Bromirski et al., 2015; Wiens et al., 2014). In this study, the focus is station DR14 (-79.142601°N, 179.947601°W), located approximately two kilometers south of the rift WR4 (Olsen et al., 2021). This station was buried ~1.5 meters below the snow surface and continuously recorded seismic motion for over 25 months (through December 2016) at a sampling rate of 200 samples per second. The full dataset was accessed via the IRIS Data Management Center. To isolate where icequakes in the record likely occurred, the data was first bandpass filtered to only include records within 5 to 20 Hz, a frequency range used in other studies of small icequakes (e.g. Lombardi et al., 2019). Next, a short-term-average/long-term-average (STA/LTA) algorithm was applied to the data record (Allen 1978; Trnkoczy 2009). Hyperparameters for the algorithm were determined per a manual review of the data in Olsen et al. (2021). The parameters found to optimize the number of detections relative to merely spurious detections were durations of 2 and 60 seconds for the short- and long- term windows respectively, and STA/LTA ratios above a threshold value of 11 that lasted for at least 0.5 seconds but no more than 10 seconds. In total, there were about 13,780 suspected icequakes found in this seismic record available to analyze in this study.

Methods

I. Initial manual identification of wave phases

Information on the arrival of body and surface waves in the seismic record are critical to identifying where the icequakes occurred relative to the seismic station. As a result, the arrival of P- and Rayleigh- waves in the icequakes has been manually labeled with the Seismic Analysis Code (SAC) program (Goldstein et al., 2003). An example of a picked event is displayed in Figure 4. Initially, 924 events were analyzed to see if wave phases could be manually identified in this initial analysis and both wave phases were identified in about 630 of the events.

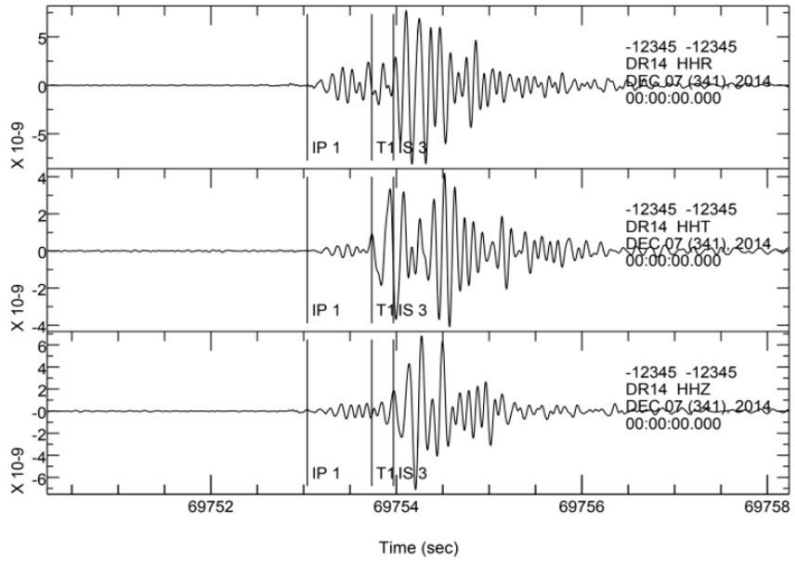

Figure 4: Eight second section of filtered seismic record from December 7, 2014, displayed in the SAC program (Goldstein et al., 2003). The P- (designated IP 1), Love- (designated T1), and Rayleigh- (designated IS 3) waves have been manually labelled.

To assist in the initial determination of wave picks, the Python library ObsPy (Beyreuther et al., 2010) has a spectrogram tool that was used to plot spectrograms for select seismic events to check if the manually picked P-wave and Rayleigh-wave time picks align with the arrivals of energy visible in a spectrogram. Adjustments were made to picks as necessary when the picked times did not appear to arrive as indicated in the spectrograms. The vertical component (HHZ) for plotted spectrograms is focused on given that the P- and Rayleigh wave arrivals would be expected to be visible. The window length of the spectrogram was determined by manual inspection to see that the possible frequencies (5-20 Hertz, thanks to the bandpass filter) were visible while maximizing time resolution. This method found 0.225 seconds to be an ideal window length. An example of a spectrogram is shown in Figure 5. In this spectrogram, the initial P-wave energy appears to enter shortly before 3 seconds (with the manual P-wave pick occurring 2.73 seconds after the start of the time window), and the Rayleigh wave (the larger amplitude energy) beginning around ~3.61 seconds.

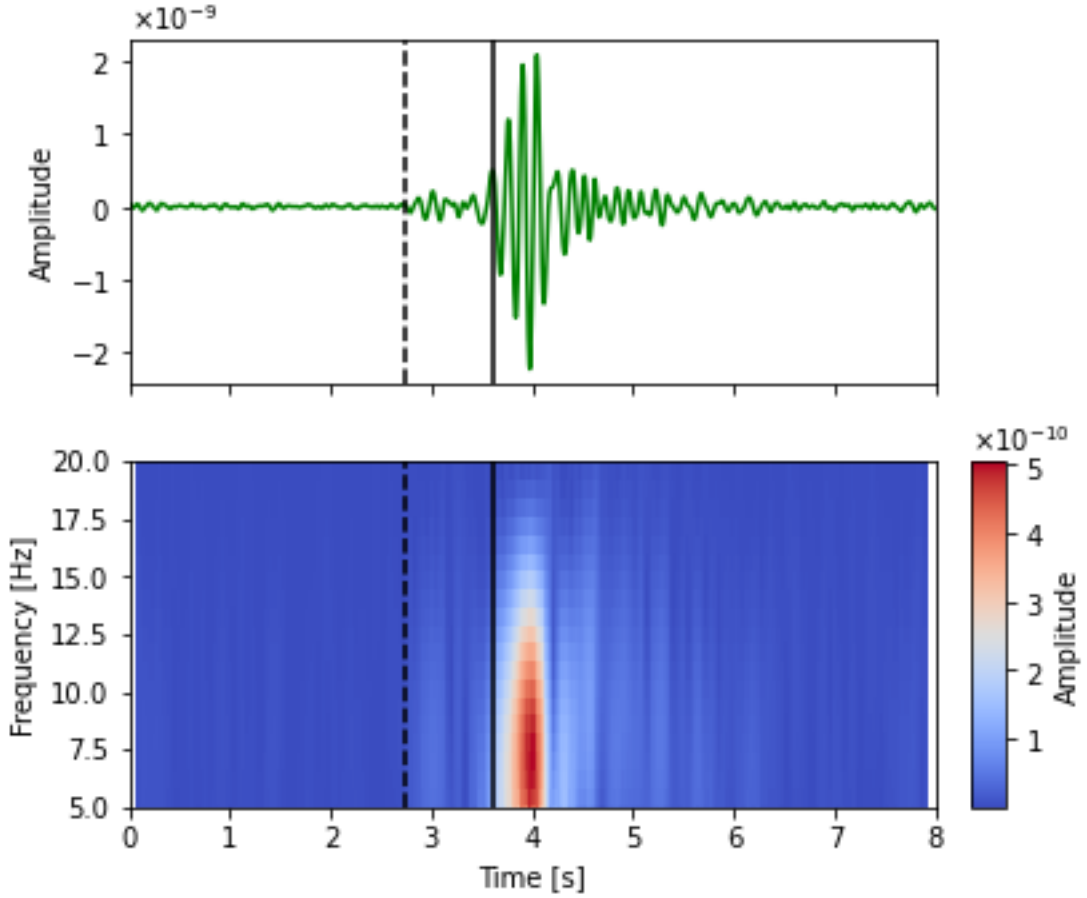

Figure 5: Seismogram (top) and spectrogram (bottom) based on vertical seismic component of data collected on an icequake with a time window of 2014-12-27 15:50:58.52 to 2014-12-27 15:51:06.52. In the spectrogram, blue corresponds to when the amplitude of energy was low, while red corresponds to higher amplitudes of energy. The dashed black line represents the P-wave arrival, and the solid black line represents the Rayleigh-wave arrival.

II. Signal Quality Analysis

Not all the labelled seismic events have equally clear signals. More accurate results regarding the distance of seismic events are expected from events with higher signal-to-noise ratios. To determine which icequakes have the clearest signal, both qualitative and quantitative approaches have been undertaken.

In the qualitative approach, each seismogram has been assigned one of four labels based on the confidence in their wave arrival picks: (1) Poor quality (2) Intermediate quality (3) Good quality, and (4) Best quality. Examples of all four types are shown in Figure 6. Events given the highest rating, “best,” tended to have little to no noise prior to the arrival of the P-wave and a Rayleigh wave amplitude far larger than the amplitude of earlier seismic energy that has reached the seismogram.

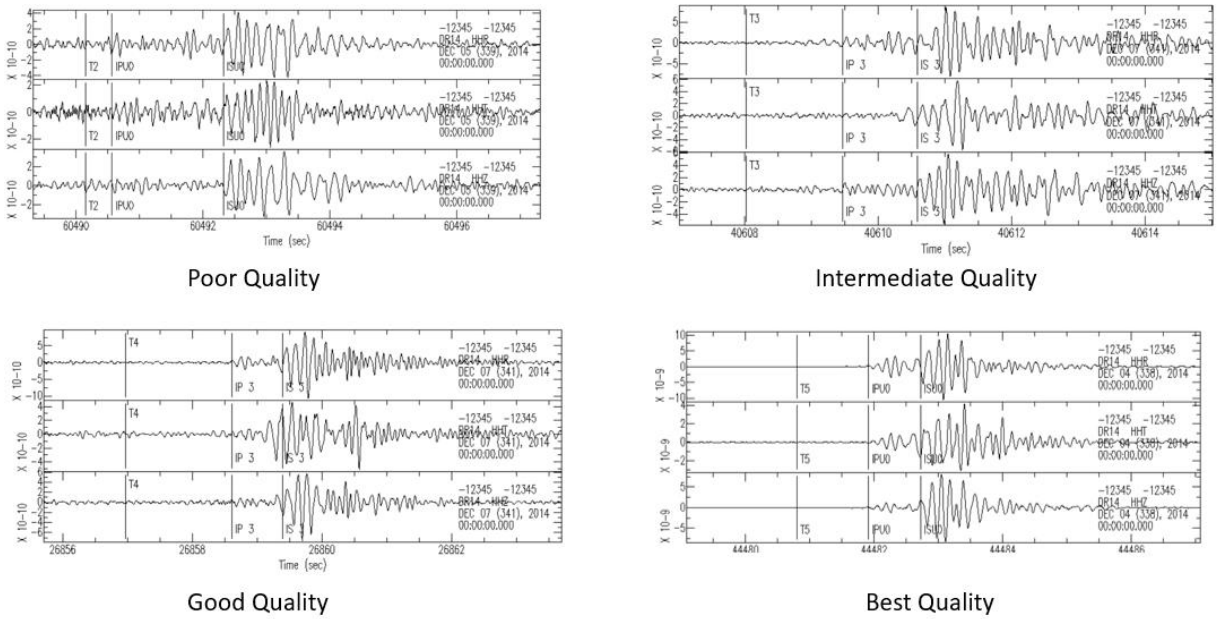

Figure 6: Examples of the four grades (poor, intermediate, good, and best) of manual quality labels assigned to the seismogram events.

In the quantitative approach, a value for the signal to noise ratio is calculated by comparing the relative amplitude of the P-wave arrival to the amplitude of the preceding signal in order to capture how distinguishable the P-wave was relative to background noise. Across the 630 events labelled, the minimum difference between the arrival and Rayleigh wave was 0.18 seconds. The signal noise window was thus determined to be in each icequake the seismic energy arrival between the labelled P-wave arrival and the minimum possible window before the Rayleigh wave energy arrives. A noise window ending 0.18 seconds prior to the P-wave and of the same length was chosen to represent the background seismic energy with the icequake arrival. The signal-to-noise ratio is then calculated with the following formula considering the logarithmic nature of the power:

$$SNR = 10 \log |\frac{S}{\sigma}| \qquad \text{[Equation 1]}$$

where SNR is the signal-to-noise ratio, S is the maximum amplitude in the signal window, and σ is the maximum amplitude in the noise window. However, the calculated SNR value was found to be highly sensitive to the length of signal and noise window chosen, so the qualitative grades were found to be more useful for consistently sorting for the best quality seismograms.

III. Stacking

By their nature, icequakes are small in amplitude. Nonetheless, the goal of this study was to confidently identify various wave phase signals in the data. As a result, the stacking methodology outlined in Shearer (1991) was followed in the initial analysis in order to improve

the signal-to-noise ratio of the data. For analysis, the focus was on the vertical (HHZ) component seismograms since it captured all relevant wave-types to the problem. First, icequakes with the lowest 10% signal-to-noise ratios were filtered out so that the results did not include less clear wave arrivals. Second, events occurring at similar distances from the seismic station (i.e., events with similar time differences between the arrival of their Rayleigh wave compared to their P-wave) were grouped together. A histogram showing the relative distribution of icequakes in bin sizes of 0.5 seconds is shown in Figure 7. Next, the waveform amplitudes for each icequake were normalized relative to the maximum amplitude in an event in their bin, making events occurring at similar distances comparable in amplitude. Each event was then aligned so that their P-wave arrivals occurred at the "zero" point on the time-axis and normalized between -1 and 1. The icequakes were then detrended to emphasize changes in their wave signals. The polarity of the P-wave arrivals in each bin was then aligned. All events in the bins were then summed together, forming stacks. The results of doing this for bin sizes of 0.5 seconds are displayed in Figure 8.

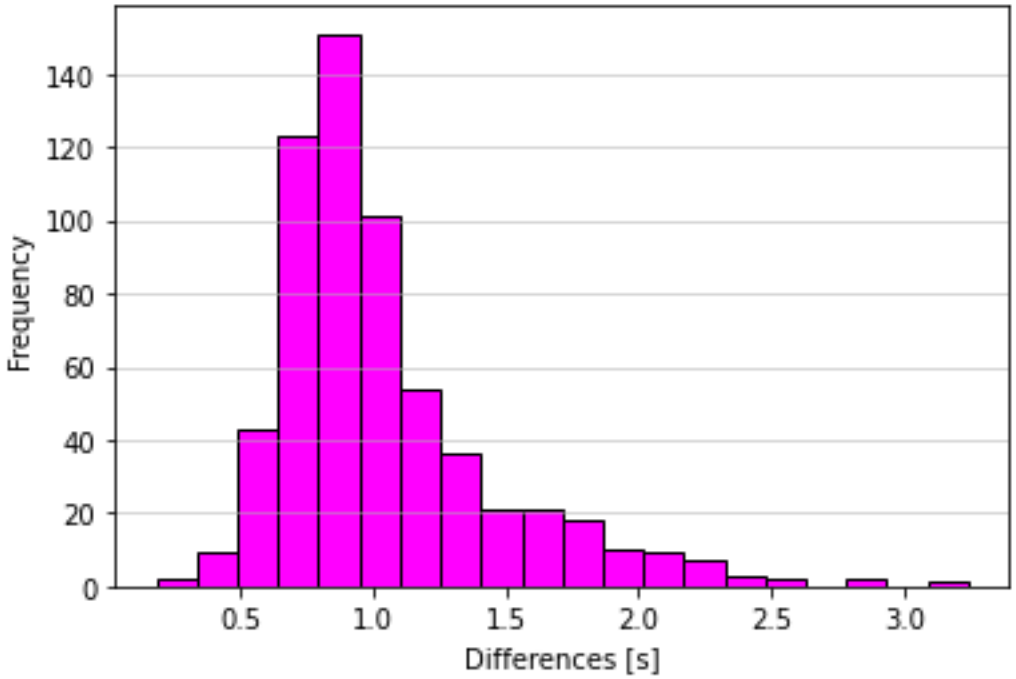

Figure 7: Histogram showing the distribution of differences in P- and Rayleigh- wave arrivals for all labeled icequake events.

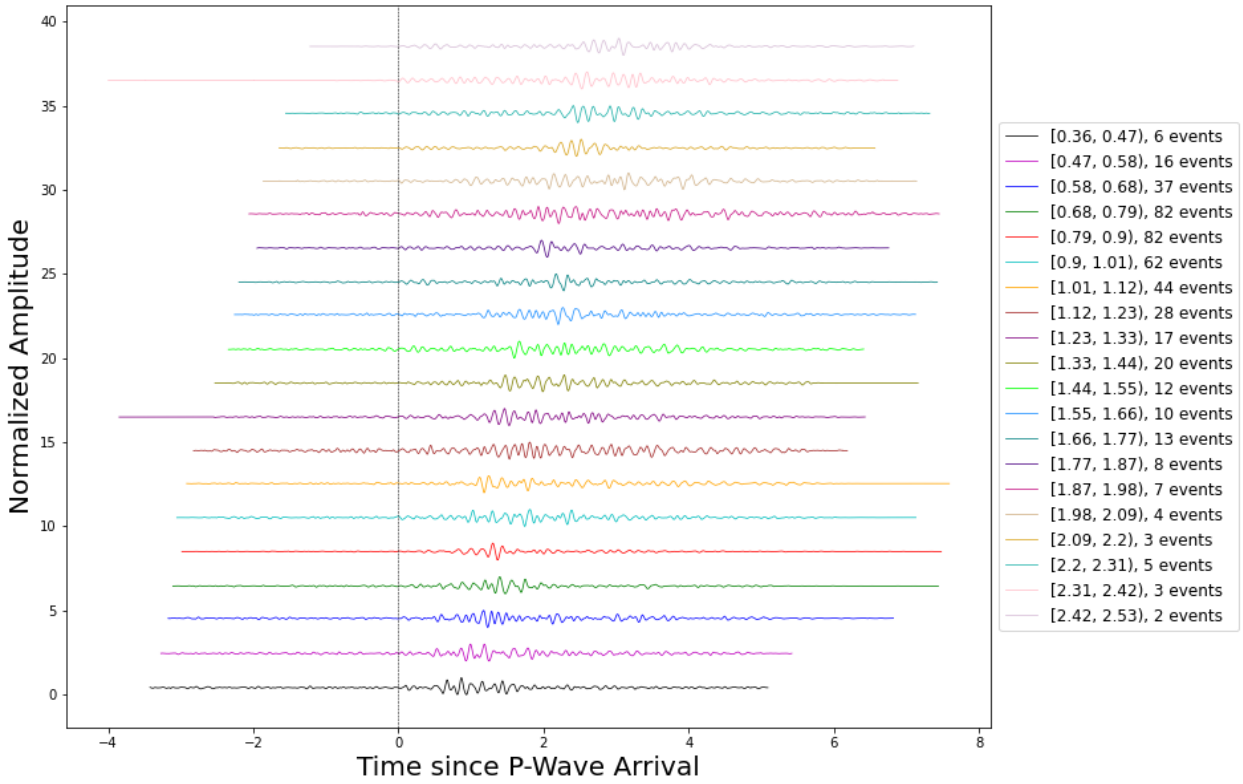

Figure 8: Example of stacked signals after icequakes were divided by similar Rayleigh- minus P- wave time differences (with a bin size of ~0.11 seconds). Stacking enables noise reduction in the data and the amplification of distinct wave phase arrivals.

IV. Velocity Modelling

The TauP Toolkit (Crotwell et al., 1999) is package of algorithms available from the University of South Carolina developed to predict theoretical arrival times for various seismic phases and has been adopted into Python via the open-source ObsPy library (Beyreuther et al., 2010). As a result, this toolkit can predict when various seismic phases would arrive given various structural parameters and distance between a seismic station and seismic source. A custom velocity model for the Ross Ice Shelf was built using a combination of crust values from PREM (Dziewonski and Anderson 1981), the P-wave seismic velocity calculated in Diez et al. (2016), and the Rayleigh-wave velocity calculated in Olinger et al. (2019). An example of several predicted wave phases interacting with the model assuming an ice thickness of 300 meters, a source depth of 200 meters (with most clear seismic signals expected to have occurred near the surface) (Huang et al., 2022), and a separation of 2 kilometers between the event source and the seismometer is shown in Figure 9. In general, the goal of this project is to locate wave phases in the seismic data that interact with the base of the ice shelf.

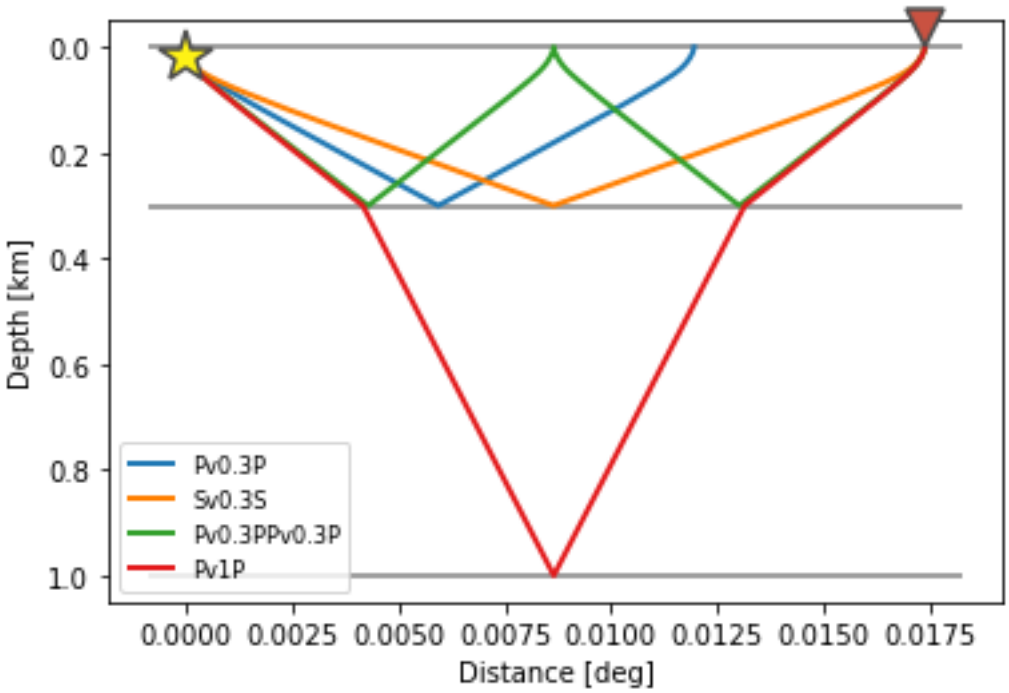

Figure 9: Predictions using a custom velocity model of the Ross Ice Shelf and TauP algorithms of the theoretical ray paths for several seismic wave phase types. The model assumes a source depth of 200 meters, a two kilometer separation between the event source and seismometer, an ice depth of 300 meters, and an ocean depth of 700 meters. The P-wave velocity was 3.8 km s^{-1} in the ice, 1.5 km s^{-1} in the water, and 5 km s^{-1} in the crust. The S-wave velocity was 1.75 km s^{-1} in the ice, 0 km s^{-1} in water, and 3 km s^{-1} in the crust. The Rayleigh-wave velocity was 1.55 km s^{-1} in the ice. The velocity values are based on Diez et al. (2016) and Olinger et al. (2019).

V. Synthetic Seismograms

Synthetic seismograms are a helpful tool to test when wave phase arrivals would be expected to arrive based on different distances from the seismometer. Applying the reflectivity methods outlined in Fuchs and Müller (1971) and Müller (1985), Figure 10 shows the cumulative result of generating synthetic seismograms generated every 25 meters out to 5000 meters (since the majority of detected events occurred within 5 kilometers) assuming various physics parameters (i.e. event source depth, P-wave velocity, Rayleigh wave velocity, thickness of ice layer, and thickness of ocean layer). The color bar corresponds to energy amplitude. The “lines” of energy shown in the figure correspond to different wave phases. By matching up the types of wave phases in the plot to a distance calculated between the seismogram and the seismic event, this is another method to predict when a specific wave phase would be expected to arrive for a seismic event. For example, in this plot and for this assumed physical structure, a P-wave wave for an event occurring 1000 meters from the seismometer appears to arrive 300 ms after the icequake

begins. This kind of plot is one way to compare expected arrival times to actual wave arrival times to find the best match in theoretical ice/ocean structure and the actual data.

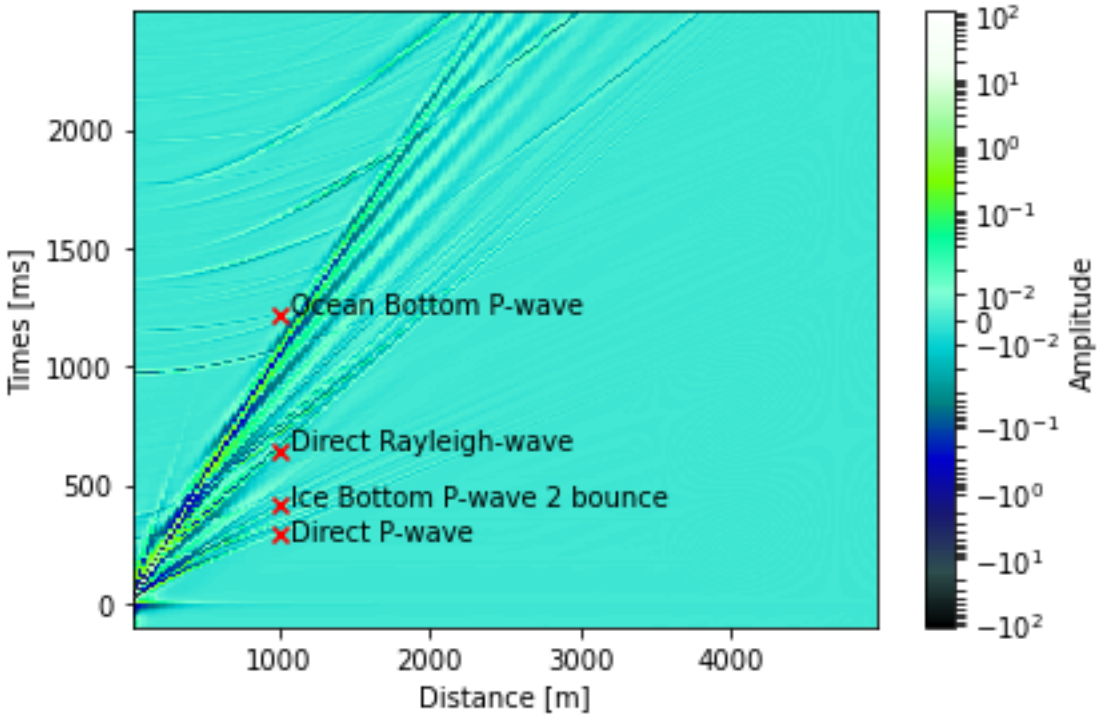

Figure 10: Cumulative results of synthetic seismograms with approximate locations of various wave phases determined by velocity modelling and visual analysis labeled with red "x" markers. Icequake source distance from the seismic station is on the x-axis, while time after the icequake is shown on the y-axis.

VI. Moveout Analysis

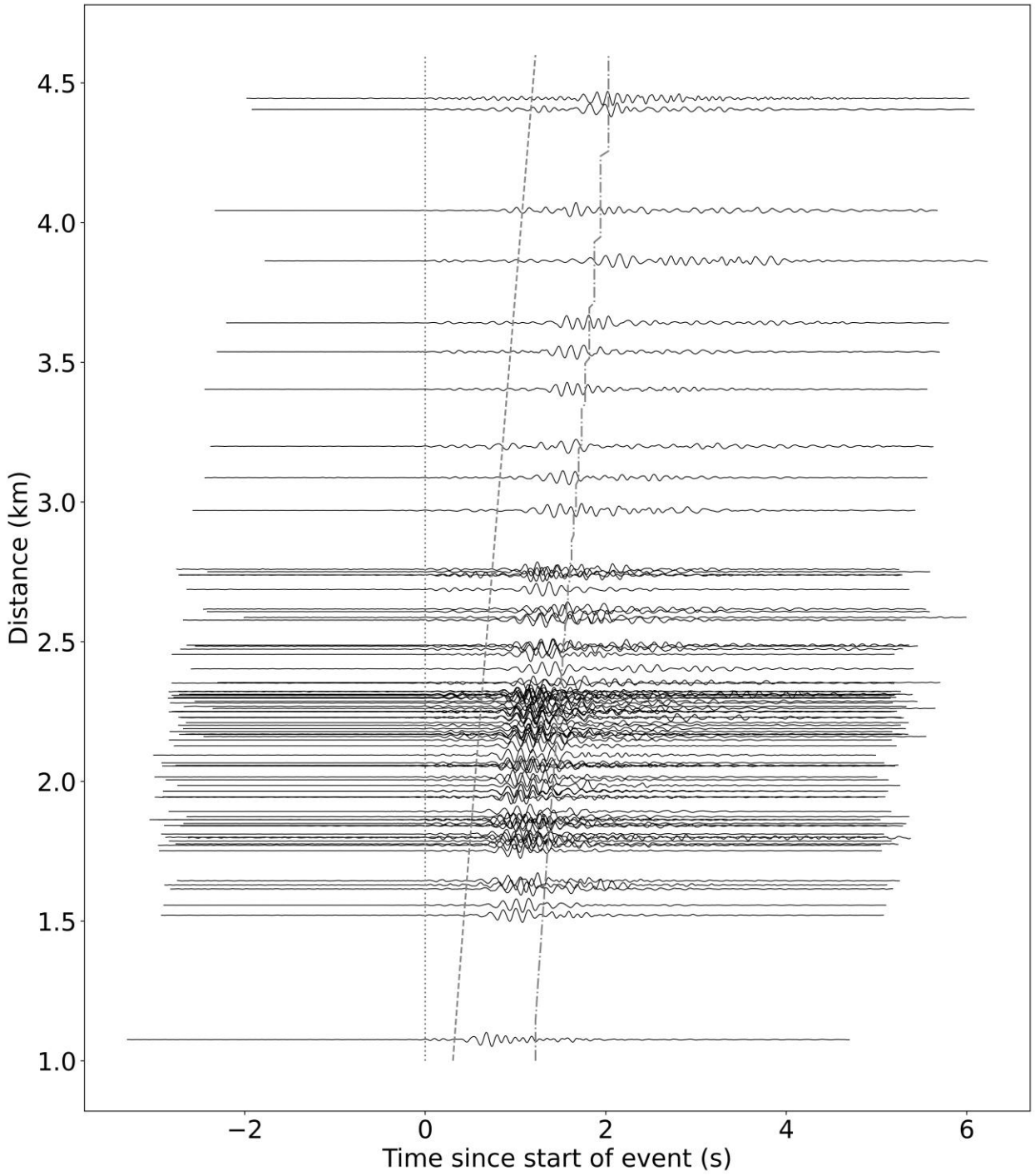

Figure 11: Eighty-five seismograms with manually labelled P-wave and Rayleigh-wave arrival times given manual "best quality" labels aligned on the time axis by their P-wave arrival time and sorted on the y-axis by their origin distance from the seismic station. The dotted line represents predicted direct P-wave arrival times. The dashed line represents predicted reflections off the bottom of the ice shelf. The dashed/dotted line represents predicted P-wave reflections from the bottom of the ocean. These predictions assume a 0.3 kilometers thick ice shelf and 0.7 kilometers thick ocean layer.

The expected arrival time of different seismic wave phase changes based on the distance between the seismometer and the seismic event source. To see if this shift can be seen in the actual data, Figure 11 is a plot showing 85 seismograms given the manual "best quality" label aligned by their P-wave arrival phases and sorted on the y-axis based on their distance from the seismometer. Although imperfect, there is a clear trend of the surface wave energy appearing to shift "right" (i.e., further after the P-wave arrival time) with increased distance from the seismometer. If moveout structure for various wave phases, including Rayleigh but also ideally wave phases that bounced off the bottom of the ice shelf, match the predicted arrival times predicted for an assumed ice structure in the synthetic seismograms, this will be an indication of the thickness of the ice shelf. Since moveout structure can be observed in individual seismograms, which are lower in quality than the stacked seismograms, this is a good indication it will be possible to infer ice (and possibly ocean) structure based on these seismic data.

VII. Polarization Analysis

Motivated by the promise of individual events being potentially sufficient to distinguish wave phases, these events were re-analyzed via a polarization analysis. Raw seismic data at these times were re-filtered by first detrending the data then applying a two-way 4^{th} order Butterworth bandpass filter with an expanded frequency range of 1.5 to 25 Hertz in case any relevant signal had been filtered out. Seismic data analyzed with the old filtering method compared to this new filtering method is shown in Figure 12. The data was then rotated to radial and transverse components to help separate the components of particle motion, something important to distinguishing types of seismic waves, using previously calculated back-azimuth values (Olsen et al., 2021).

Polarization analysis allows identification of the seismic wave type based on the signal's particle motion (Stähler et al., 2021). The data was initially inspected by plotting the three components (vertical, radial, and transverse) over spectrograms formed from these re-filtered waveforms. The sampling interval was set to four samples at the highest frequency (25 Hertz). The resulting waveforms and spectrograms are shown in Figure 13. Windows of suspected wave arrivals (generally those for P-waves and Rayleigh waves) were selected (as shown in Figure 14a) to undergo frequency dependent polarization analysis (Park et al., 1987). In particular, this study followed the approaches outlined in Goodling et al. (2018) and Stähler et al. (2021) since these studies outline the specific application of frequency dependent polarization analysis to single station seismology. For a detailed description of the methodology, readers are referred to these works.

The calculated 3D particle motion was plotted as shown in Figure 14b since the polarization of seismic signals corresponds to characteristic particle motion (Stähler et al., 2021). For example, P-waves are rectilinearly polarized while Rayleigh waves tend to be elliptically polarized. If the plotted particle motion matches the expected nature of particle motion for the

suspected wave arrival region, this is a strong sign of that type of wave arrival in the selected region.

Hodograms are also a way of plotting particle motion in a particular time window. As shown in Figure 14c, hodograms were plotted comparing the relative motion of particles in the radial, transverse, and vertical components to particles in the other components. The top left plot of Figure 14c shows the waveform and how the colored (blue-yellow) time axis aligns to the waveform. The top right plot of Figure 14c plots the relative motion of the vertical and radial components (with colored points corresponding to the time of the particle motion). The bottom left plot of Figure 14c plots relative vertical-transverse motion and the bottom right plot shows transverse-radial motion. Uncertainties in the back-azimuth values did lead to particle motion of particular seismic wave types not always completely isolated to expected components.

The polarization attributes were calculated via the equations outlined in Goodling et al. (2018). Potential wave arrivals had a high average horizontally rectilinear motion (HRM and vertically rectilinear motion (VRM) across various frequencies (Stähler et al., 2021; Quancheng et al., 2022). The top plot of 14d shows a plot of VRM over time across the given frequency range while the middle plot shows likewise for HRM. The polarized waveforms for all three components were then computed the same way as those in Quancheng et al. (2022) and the result is shown in the bottom plot of Figure 14d. The polarized waveforms help to emphasize potential wave arrivals and suppress noise and scattered waves that lack rectilinear polarization (Quancheng et al., 2022), enabling more precise arrival pick times.

(a) 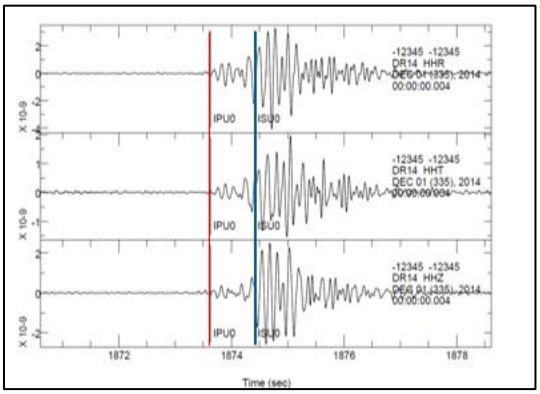

(b) 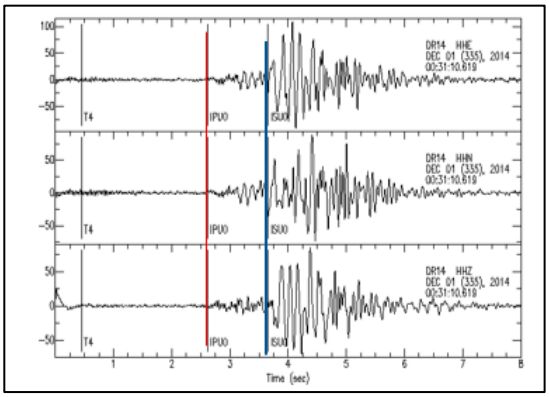

Figure 12: (a) Data filtered to 5-20 Hz. (b) Data filtered to 1.5-25 Hz.

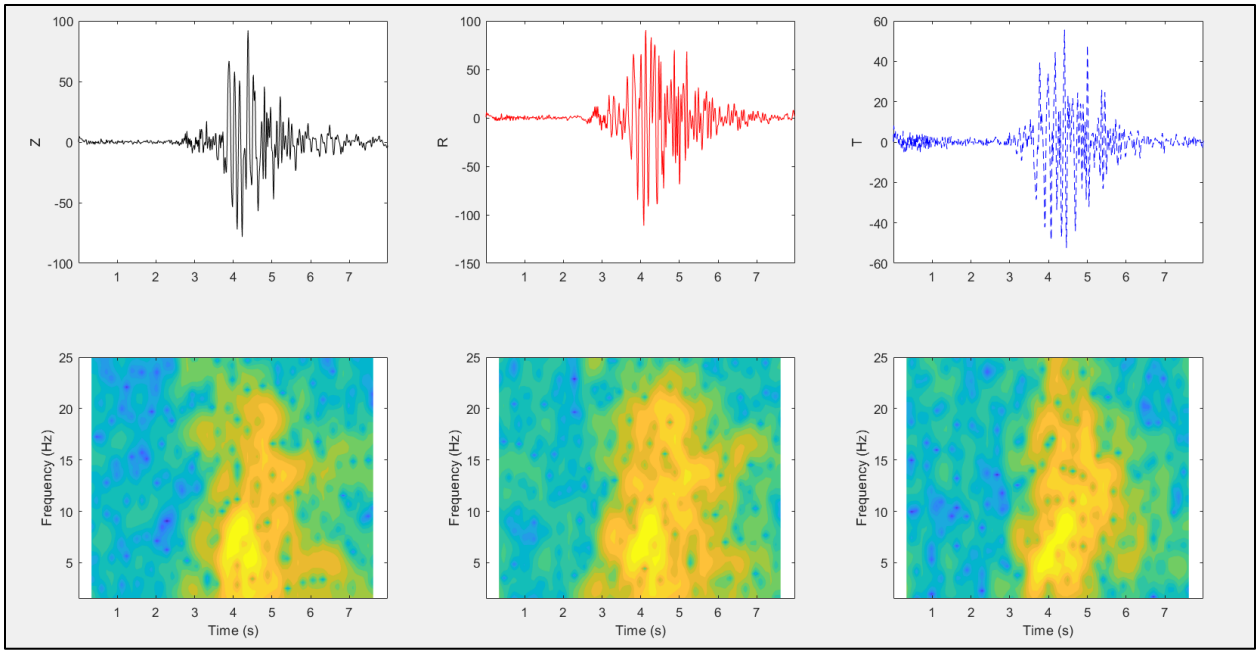

Figure 13: Initial seismograms and spectrograms split by the three components (Z, R, and T) where the data has been rotated by the previously calculated back-azimuths. Rayleigh wave arrivals tended to occur close to 10 Hz while P-wave arrivals were looked for at higher frequencies.

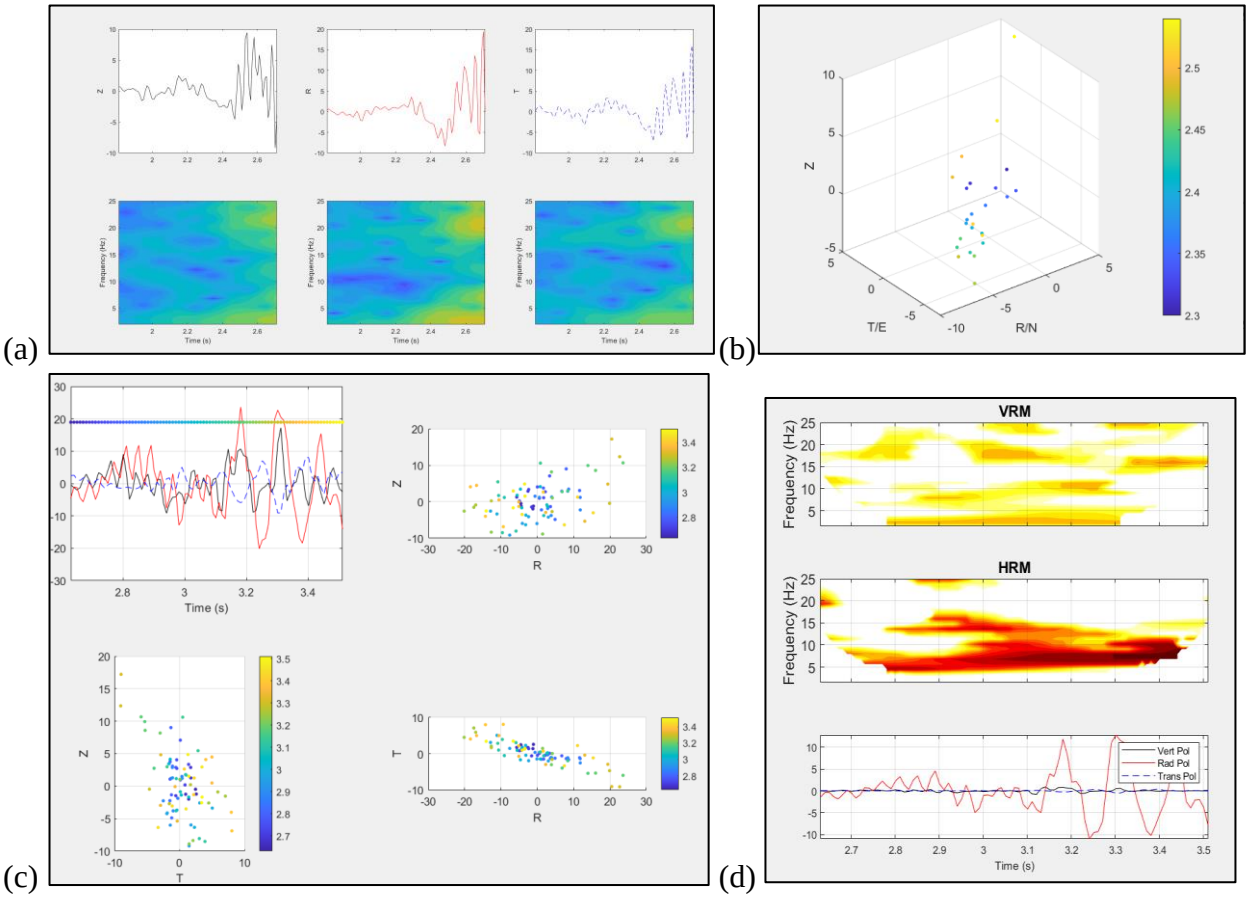

Figure 14: Results of frequency-dependent polarization analysis. (a) Seismograms and spectrograms from the Z, R, and T components examined in this analysis. (b) 3D particle motion. (c) Relative motion between the Z, R and T components. The upper left plot shows for reference the seismogram in this time window. (d) Polarization attributes from frequency-dependent polarization analysis. The VRM plot shows rectilinearly polarized motion in the vertical direction while the HRM plot shows horizontal rectilinear motion (HRM). Candidate wave arrivals generally have higher average HRM/VRM across different frequencies for a given time. The bottom plot shows the polarized waveforms.

Results

I. Event Distance Distribution

Using previous estimates of P- and Rayleigh- wave velocities (v_P and v_R, respectively) in the Ross Ice Shelf, the distance (d) at which these events occurred relative to the seismic station can be estimated via the following formulas:

$$T = t_R - t_P \quad \text{[Equation 3]}$$

$$V = \frac{1}{v_R} - \frac{1}{v_P} \quad \text{[Equation 4]}$$

$$d = \frac{T}{V} \quad \text{[Equation 5]}$$

where t_R is the time the Rayleigh wave arrived and t_P is the time the P-wave arrived. Subsequent error on the distance measurements (σ_d) could be calculated by:

$$\sigma_T = \sqrt{\left(\sigma_{t_P}\right)^2 + \left(\sigma_{t_R}\right)^2} \quad \text{[Equation 6]}$$

$$\sigma_V = \sqrt{\left(\frac{\sigma_{v_P}}{v_P^2}\right)^2 + \left(\frac{\sigma_{v_R}}{v_R^2}\right)^2} \quad \text{[Equation 7]}$$

$$\sigma_d = \sqrt{\frac{T^2\sigma_V^2 + V^2\sigma_T^2}{V^4}} \quad \text{[Equation 8]}$$

where σ_{t_P} is the error on the P-wave arrival, σ_{t_R} is the error on the Rayleigh-wave pick, σ_{v_p} is the error on the P-wave velocity, and σ_{v_R} is the error on the Rayleigh-wave velocity. Olinger et al. (2019) calculated the Rayleigh wave velocity of the Ross Ice Shelf with the same seismic network to be approximately 1.55 ± 0.05 m s^{-1}, and Kirchner and Bentley (1979) estimated the P-wave velocity to be 3.80 ± 0.05 m s^{-1}. To determine the error on the P-wave and Rayleigh-wave picks, the sampling rate of the seismic data, 0.005 seconds, was the first factor taken into consideration. Next, 12 seismograms were picked at random. In them, windows where there could have been possible P-wave and Rayleigh-wave picks were manually identified, and this yielded results of 0.079 seconds and 0.100 seconds respectively. These two types of errors were summed, setting the value of σ_{t_P} to 0.084 seconds and σ_{t_R} to 0.105 seconds. After applying this

to all labeled events, the average event was found to have occurred 2.7 ± 0.4 kilometers from the seismometer.

Olsen et al. (2021) calculated the azimuths (angle relative to the seismometer) for the same dataset using a technique developed specifically for a single seismometer (Baker and Stevens, 2004) involving surface wave polarization. By combining calculated distances, azimuths, and known seismometer location, coordinate locations of the seismic event sources were found using a standard geodetic formula. Figure 15 displays the distribution of seismic events relative to the seismic station over an image of the rift WR4 taken via 2013-2014 MODIS imagery (Haran et al., 2018). The map clearly shows the vast majority of events occurred along the WR4 rift. However, a limitation of interpreting the distribution of events relative to the rift is that the Ross Ice Shelf is in motion over time, and the velocity of the ice relative to the DR14 station was found over 2015-2016 to move 902.51 meters year^{-1} so plotting the exact location of the seismometer relative to the current location of the shelf is limited by image time resolution and the time distribution of events (Klein et al., 2020). All currently labeled events occurred between December 2014 and February 2015.

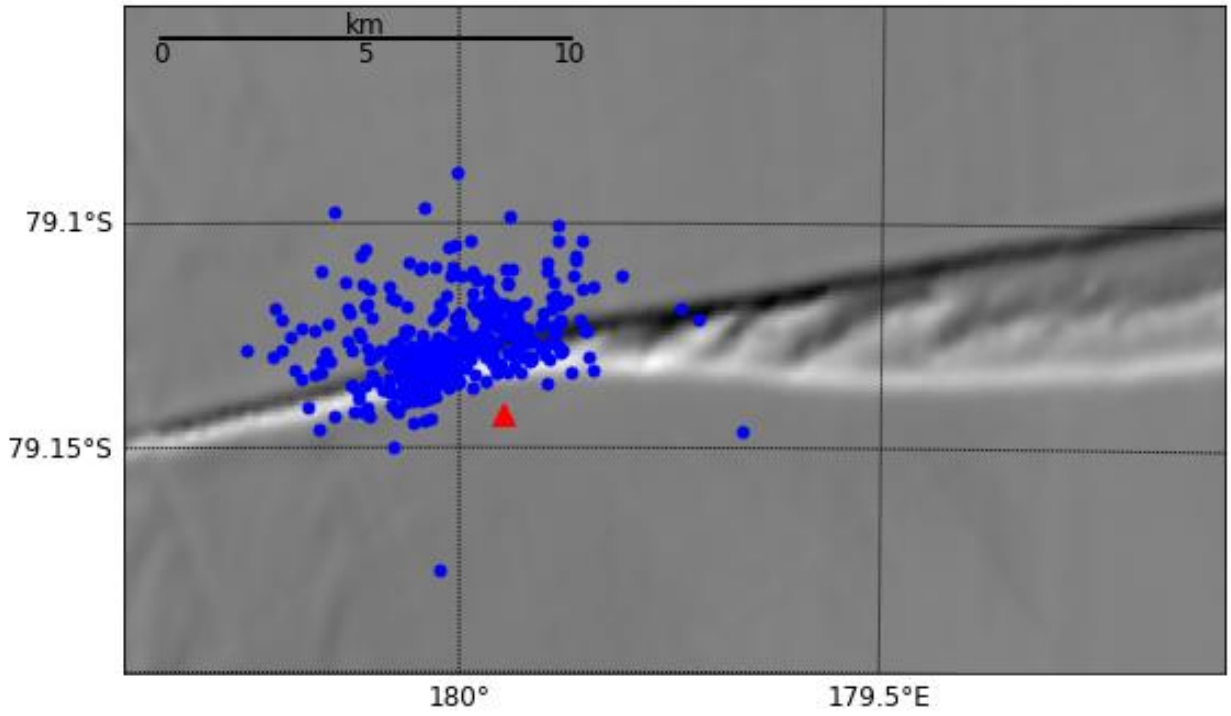

Figure 15: Map of the distribution of seismic events using an Antarctic Polar Stereographic projection. Overlapped over image of rift WR4 from MEaSUREs MODIS Mosaic of Antarctica 2013-2014 (Haran et al., 2018). The seismometer is represented by a red triangle while the icequake events are represented by blue circles.

II. Predictions of seismic wave phases

Using the custom velocity model developed for the ice shelf, arrival times of different seismic phases can be calculated for individual and/or stacked seismograms by computing the distance between the seismic event and the seismometer and assuming the thickness of the ice shelf, the thickness of the ocean layer, and depth of the seismic event source can be calculated for custom seismograms. An example of this applied to an individual seismogram is shown in Figure 16. Even though this is only a single seismic event, the predicted P-wave and Rayleigh wave arrivals appear upon manual inspection to visually match up with seismic energy arrivals in the seismogram. This means that the specified assumed parameters in this case would be consistent with observed seismic wave phase arrivals. The goal is to apply this to highest-quality seismic events and the stacked seismograms to see what ice shelf parameters yield results that match observed seismic wave arrivals with predicted wave phase arrivals based on those parameters. Wave phase arrivals that have interacted with the bottom of the iceshelf (e.g. Pv0.3P) are of particular interest.

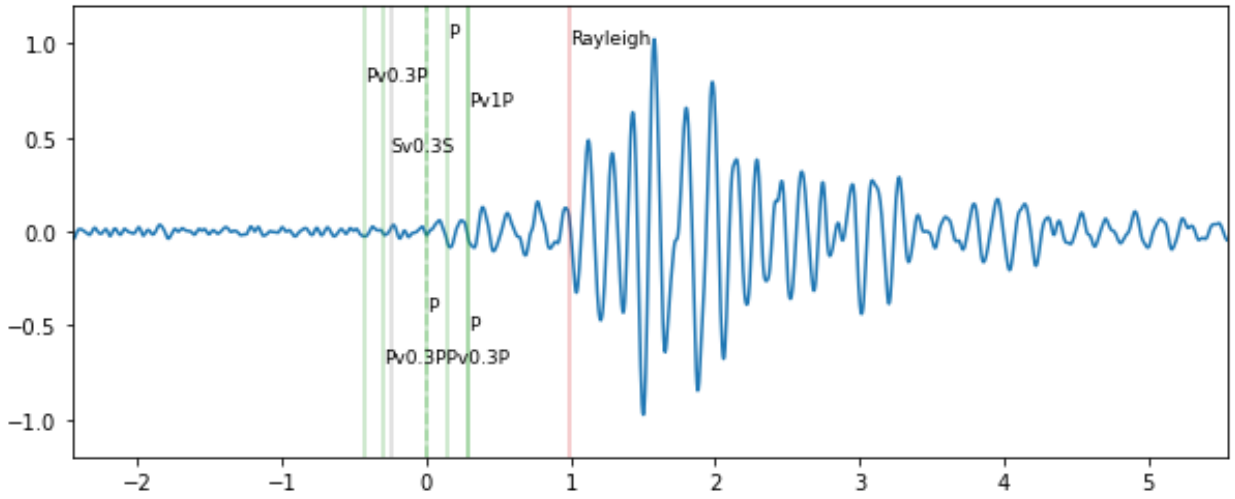

Figure 16: Predicted wave phase arrivals (indicated by dashed and solid lines) for the P-wave, Pv0.3P, Sv0.3S, Pv1P, Pv0.3PPv0.3P, and Rayleigh phases (similar wave phases to those shown in Figure 9) calculated using a TauP model for a seismic event occurring at 2014-12-07 16:35:13.

III. Vespagram analysis

To further assist in determining the ice shelf structure, we applied the method of velocity spectral analysis (vespa) (Davies et al., 1971). When plane waves arrive at the seismic station, the recorded signal has a certain time offset affected by the source-station separation distance and the slowness of the wave (Rost and Thomas, 2002). These time-offsets can be used in the vespa process to help determine unknown horizontal slowness or back azimuth (components of slowness vectors) of an arriving seismic signal so long as there is input of either the horizontal slowness or back azimuth (Rost and Thomas, 2002). The output of the vespa process is a vespagram, a plot showing the amplitudes of incoming seismic signals as a function of slowness and time (Rost and Thomas, 2002).

Since arrivals were generally strongest on the radial component, seismic data from this component was the subject of the analysis. Of the seismic events reanalyzed with frequency dependent polarization analysis, vespa analysis was performed on only 65 events given the top manual pick confidence tier for both their P-wave and Rayleigh-wave arrival time. These events occurred an average of ~4.1163 kilometers away from the seismic station, shown in Figure 17. For the vespa prcess, the seismic data was first arranged into a regular matrix. Using their calculated distances (based on their wave arrival picks), the events were initially sorted by distance with each seismic event's amplitudes normalized. The resulting stacks are shown in Figure 18. Figure 18a shows the distribution of the strength of seismic signals over time at different distances and Figure 18b shows the result of summing the seismic signals when aligned by their P-wave arrival. Next, the travel times are calculated for a plane wave arriving at the seismic station. Array beam forming (as described in Rost and Thomas, 2002) is used to separate the signal and noise components of the seismic signal. With the technique, if the seismic data is shifted in time for a specific back azimuth (assumed constant here) and slowness, the signal should constructively add together.

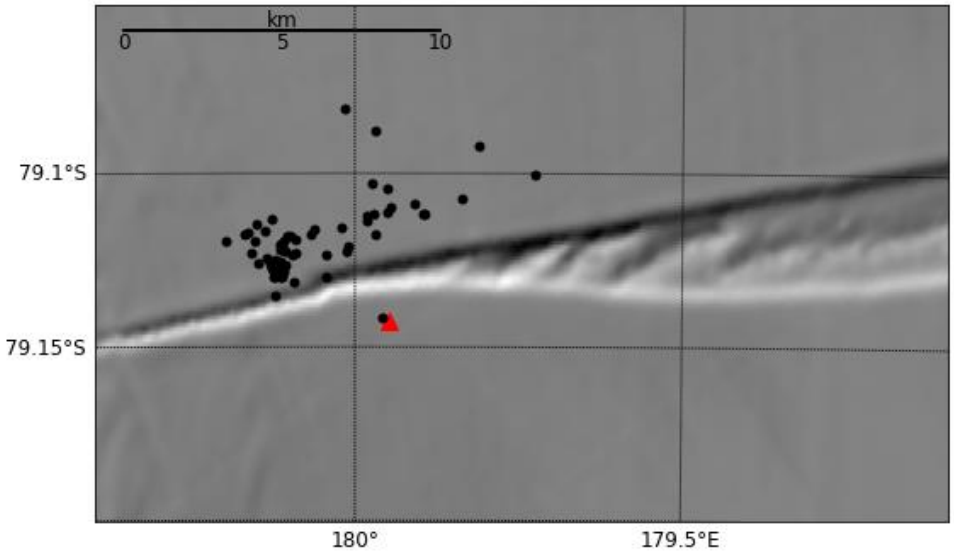

Figure 17: Similar to Figure 15, but shows the distribution of the event distances (black dots) from the seismic station (the red triangle) for the seismic signals re-analyzed with frequency-dependent polarization analysis and vespa.

The vespagram, seen in Figure 19a, is then plotted showing the stacked amplitude of the beam form over time for different slowness values. Predicted arrival times of several wave phases were then calculated using the same Ross Ice Shelf TauP model used discussed in the velocity modelling section. The predicted arrival times for these various phases are labelled both in regards to the vespagram in Figure 19a and to the stacked waveform in Figure 19b. Although further finetuning is needed, the predicted wave phase arrivals do visually appear to be correlated with frequency changes in the waveform (something polarization analysis could confirm). Most

importantly, the predicted wave arrival times are close to coherent signals in the vespagram, indicating the predicted structure is close to that used in the TauP model, with an ice shelf thickness of approximately 300 meters.

To calibrate the vespa analysis process, it was also performed on the synthetic data generated as described in the synthetic seismogram section (shown in Figure 20). The distinct wave arrival signals are much clearer in the synthetic data's vespagram (Figure 20a) than the vespagram of the real data (Figure 19a). However, the timing of the various predicted seismic phases is similar between the synthetic and actual data (e.g., PV0.85S arriving slightly one second after the initial P-wave arrival) indicating the structure used to calculate the synthetic data is similar to that leading to the actual data. Nevertheless, the average distance the synthetic seismic events occurred was 3.5234 kilometers, so an ideal comparison between the synthetic and real data would have the synthetic events having a similar time offset distribution. In doing so, further analysis could be done to see how changing the modeled Ross Ice Shelf structure enables closer matches between the predicted wave phase travel times and actual wave phase travel times.

(a)

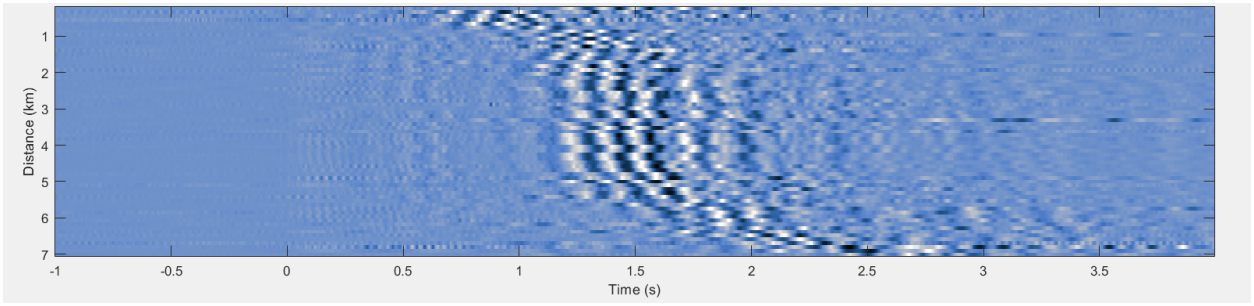

(b)

Figure 18. Aligning 65 seismic events whose P-wave and Rayleigh-wave arrival times were determined using frequency-dependent polarization analysis by their P-wave arrival time (t=0 seconds). (a) Arrival of seismic energy from different distances over time. (b) Summed stack of the normalized amplitude aligned seismic data.

(a)

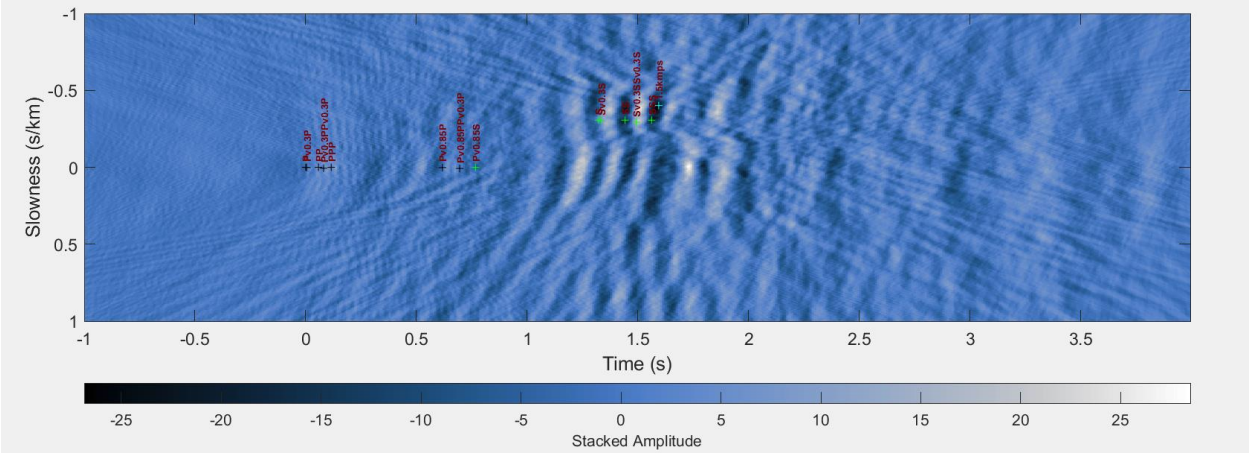

(b)

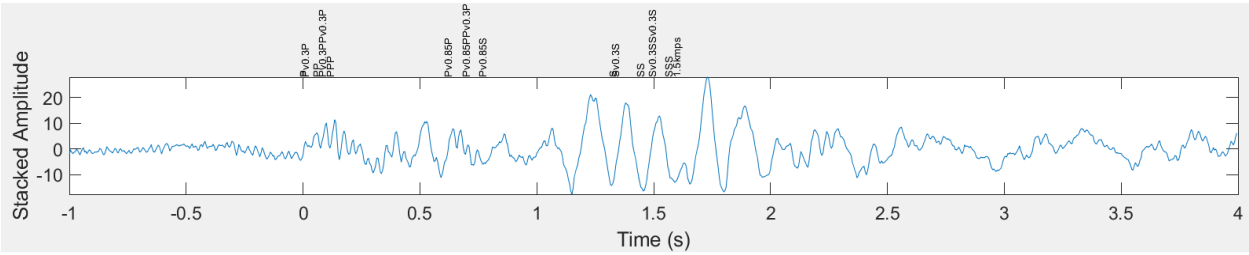

Figure 19: Result of vespa analysis for the 65 aligned seismic events. (a) Vespagram with labeled predicted seismic phases calculated from the velocity model. (b) Predicted wave arrivals in relation to the stacked seismic waveform.

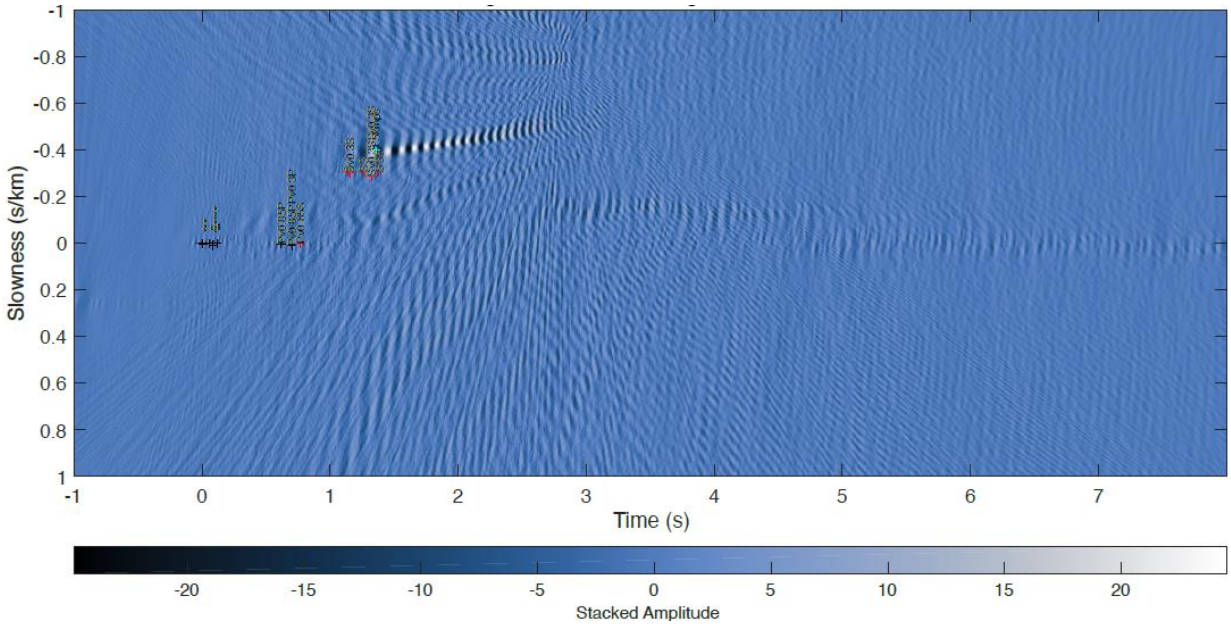

(a)

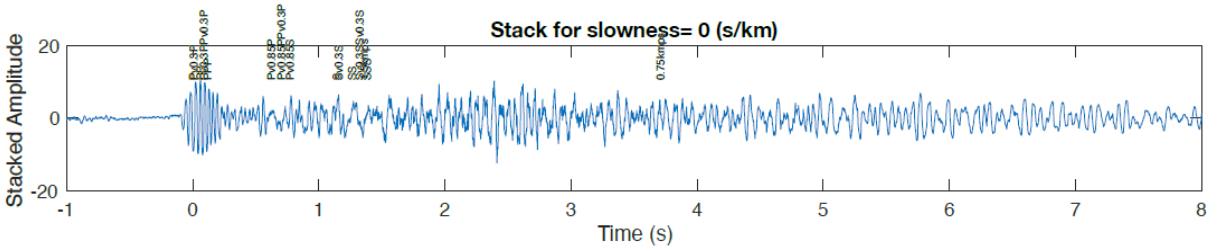

(b)

Figure 20: Vespagram for synthetic seismic data calculated for every 25 meters out to 5000 meters. (a) Vespagram with overlain predicted wave arrival times for the current velocity model. (b) Predicted wave phase arrivals labelled on the stacked seismic waveform constructed from the synthetic seismic signals.

Discussion

Early comparisons between the synthetic and actual seismograms indicate that it will be possible to predict both ice and sub-glacial structure from the seismic data collected by the DR14 station. More comparisons should occur between the actual data and the synthetic seismograms predicted for different potential structures to find the structure that most closely predicts similar wave phase arrival times. It remains to be seen how precise the results for ice shelf thickness will since the current coarse resolution being used for such models would not yet permit this kind of analysis. The analysis that has occurred thus far is based only on three months of data (December 2014-February 2015), so it could also be interesting to see if any changes in the thickness of the ice shelf will be visible in these data by comparing the results obtained at the beginning of the data collection period to those at the end (e.g. around November-December 2016). Brief examination of derived ice densities from ROSETTA mission data (Das et al., 2019) appears to show small changes from 2015 to 2016, displayed in Figures 21a and 21b, respectively. However, differences in data spatial coverage between the two years does need to be accounted for. Nevertheless, the WR4 rift in this study appears to be roughly located between areas of slightly higher density and slightly lower density and changes in that density could possibly affect fracturing and thermal processes.

The ice shelf thickness results suggested by airborne ice-penetrating radar (e.g. Das et al., 2020) of approximately 300 meters (see Figure 2) is the same thickness able to generate a velocity model of the Ross Ice Shelf that can roughly match observed wave phase arrivals. As a result, this helps support the feasibility using a single seismic station in cryospheric settings to learn more about underlying structure. Further comparisons of the ice shelf structure could be made to radar altimetry data (e.g. Hogg et al., 2021) in the future. These comparisons lend insight into the accuracy of the methodology. However, more work should be done to see how much the depth in the Tau-P velocity model and structure parameters can be varied when generating synthetic seismograms and still end up with similar predictions of wave phase arrivals.

Moreover, to support planetary analog applications, synthetic seismograms based on the physical parameters predicted for an icy ocean world such as Enceladus could be generated. In doing so, one can see if characteristic wave phase(s) identified as corresponding to the thickness of the ice shelf are expected to be visible in seismic data collected on such a world. However, there are various limitations of comparing the Ross Ice Shelf to Enceladus so comparisons would need to be made between the various physical parameters used to generate synthetic Enceladus data and those of the Ross Ice Shelf.

Another method proposed to determine ice-shelf thickness using a single seismometer is to look for trapped Crary waves in the seismic signal (Panning et al., 2018; Marusiak et al., 2021). The Crary method has the advantage of not necessarily needing clear identification of wave phases (Stähler et al., 2018). However, the methodology explored in this paper involving body waves could allow exploration as to whether ice shells vary on regional and/or global scales since wave travel paths need to be known for that kind of analysis (Marusiak et al., 2023).

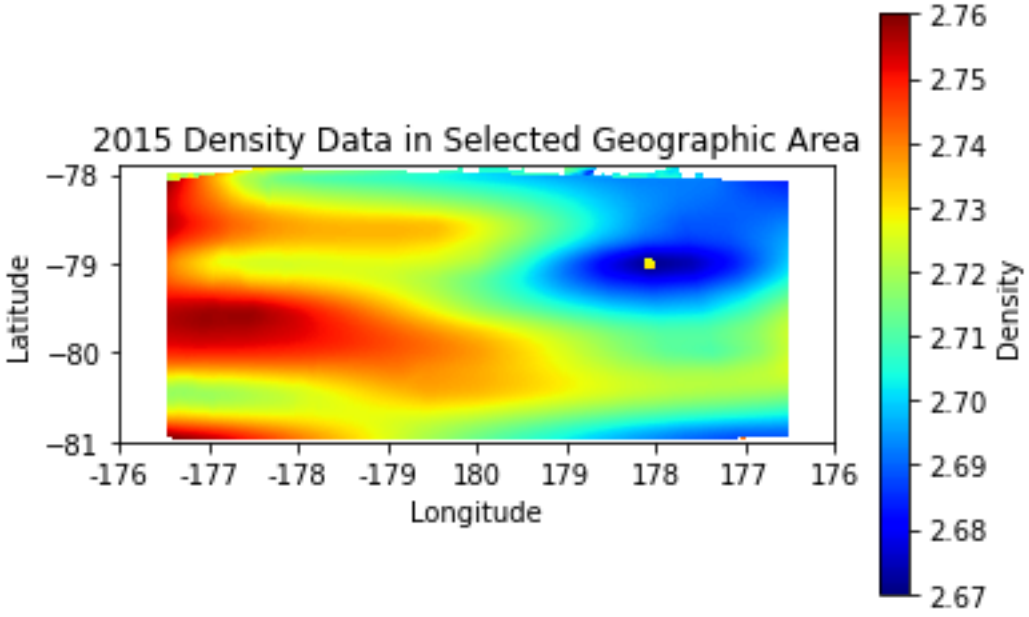

(a)

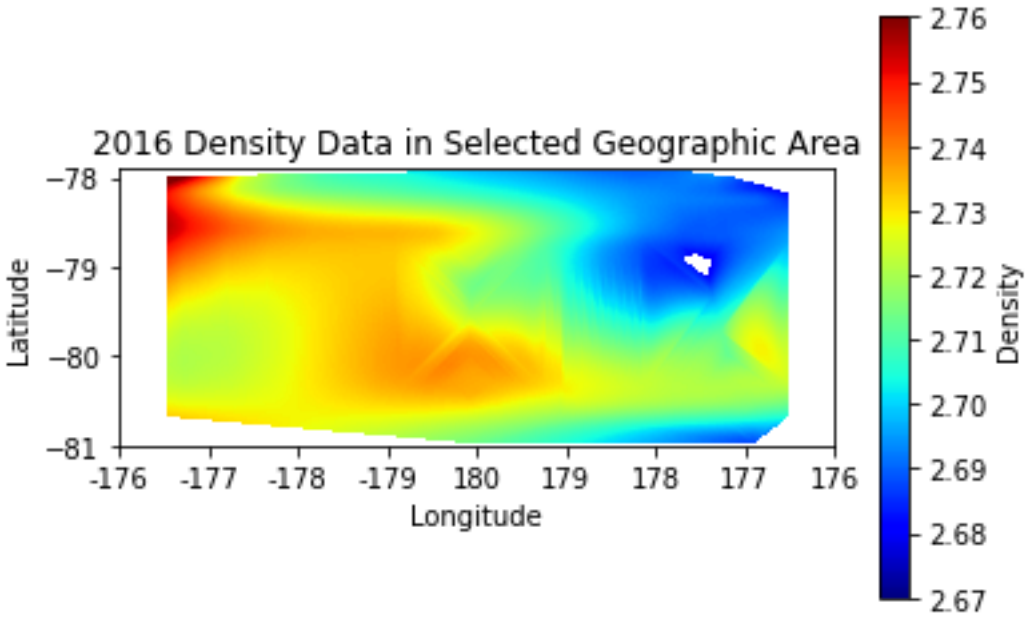

(b)

Figure 21: Derived ice densities (based on derived ROSETTA data from Tinto et al., 2019) for (a) 2015 and (b) 2016 in proximity to the study area (the WR4 rift is located 79.142601°N, 179.947601°W).

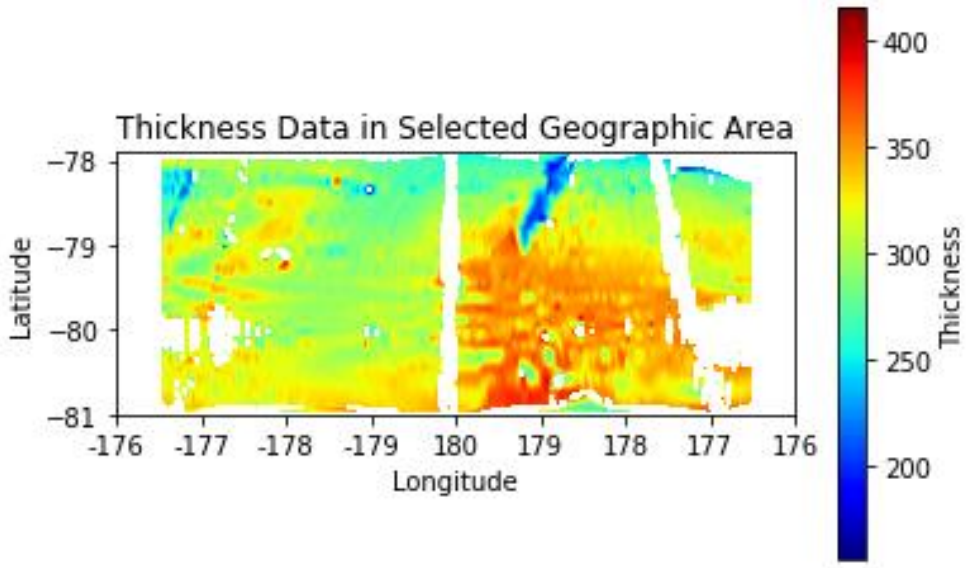

Figure 22: Map of the derived ice thickness data (Das et al., 2020) from the ROSETTA mission's DICE radar. The ice thickness data was cleaned of outliers leading to some spatial gaps. However, variation of >200 meters in ice thickness occurs within relative proximity to the study area (the WR4 rift is located 79.142601°N, 179.947601°W).

An insufficient amount of seismic phase arrivals was identified with polarization analysis to enable sufficient spatial resolution to find a gradual transition occurs at the ice-ocean interface. As a result, the null hypothesis of a sharp transition from the ice shelf to the ocean is all the current structure model supports. However, analysis of far more well-resolved events than the

current 65 could stand to change that result. Furthermore, future work could be done involving analysis of the polarization of wave phases (like the P-wave) to see if this can give insight into the mechanics generating the seismic signals observed in the data, and whether such mechanics would be expected somewhere like Enceladus. When considering potentially taking insights from this study to understand the ice-ocean interfaces of icy ocean worlds, an important limitation to keep in mind is that the timescales of freezing processes that may occur beneath terrestrial ice shelves are likely orders of magnitude faster than those at the bottom of icy shells (Vance et al., 2021; Wolfenbarger et al., 2022).

Summary

In this study, seismic data recorded by a single seismometer was analyzed to find distinguishable reflections off the water-ice interface related to the thickness of the ice shelf. The null hypothesis is that there exists a sharp transition at the ice-ocean interface while the alternative hypothesis is that a more gradual, complex transition is occurring. To do so, P-wave and Rayleigh-wave arrivals have been manually identified in seismograms. Frequency-dependent polarization analysis has enabled more accurate identification of specific wave phase arrivals. Information regarding wave phase arrivals in turn enables the calculation of the distance between where those seismic events occurred and the seismometer. Using the TauP toolkit and a custom-built velocity model for the Ross Ice Shelf, these distances can be used to make predictions about the timing wave phase arrivals for various seismic phases (including those that bounce off the bottom of the ice shelf) for different potential ice shelf velocity structures. The predicted wave phase arrivals are compared to the observed seismograms via the vespa process to see if similar wave phase predictions occur for a given ice shelf structure. Synthetic seismograms based on an assumed physical structure can also be used to predict when different seismic wave phases are predicted to arrive in seismic signals. Comparisons between this and the actual change in times of wave phase arrivals for icequakes occurring at different distances help determine the predicted underlying structure. Current data analysis based on velocity modelling and synthetic seismograms indicates that ice and ocean structure can be determined based on this data. Nevertheless, relatively few high-quality seismic events have had manually identified body and surface waves so only a sharp ice-ocean-crust structure can be identified at this time. Analysis of far more seismic events could possibly find regional variation in the structure of the iceshelf, including at the ice-ocean interface but no such variation can be identified at this time.

Acknowledgements

I would like to acknowledge my advisor Dr. Nicholas Schmerr for making this project possible and spending many hours teaching me about seismology. I would also like to thank Kira

Olsen for guiding me through the initial stages of the project. I also appreciated the assistance of Vedran Lekic for helping provide code and guidance for the polarization analysis. I am also grateful for the help of Mong-han Huang for feedback on mapping the icequake locations.

References

Allen, R. V. (1978). Automatic earthquake recognition and timing from single traces. Bulletin of the Seismological Society of America, 68(5), 1521-1532.

Aster, R. C., Lipovsky, B. P., Cole, H. M., Bromirski, P. D., Gerstoft, P., Nyblade, A., ... & Stephen, R. (2021). Swell-triggered seismicity at the near-front damage zone of the Ross Ice Shelf. Seismological Research Letters, 92(5), 2768-2792.

Baker, G. E., & Stevens, J. L. (2004). Backazimuth estimation reliability using surface wave polarization. Geophysical Research Letters, 31(9).

Beyreuther, M., Barsch, R., Krischer, L., Megies, T., Behr, Y., & Wassermann, J. (2010). ObsPy: A Python toolbox for seismology. Seismological Research Letters, 81(3), 530-533.

Bromirski, P. D., Diez, A., Gerstoft, P., Stephen, R. A., Bolmer, T., Wiens, D. A., ... & Nyblade, A. (2015). Ross ice shelf vibrations. Geophysical Research Letters, 42(18), 7589-7597.

Brunt, K. M., King, M. A., Fricker, H. A., & MacAyeal, D. R. (2010). Flow of the Ross Ice Shelf, Antarctica, is modulated by the ocean tide. Journal of Glaciology, 56(195), 157-161.

Buffo, J. J., Schmidt, B. E., Huber, C., & Walker, C. C. (2020). Entrainment and dynamics of ocean-derived impurities within Europa's ice shell. Journal of Geophysical Research: Planets, 125(10), e2020JE006394.

Buffo, J. J., Schmidt, B. E., Huber, C., & Meyer, C. R. (2021). Characterizing the ice-ocean interface of icy worlds: A theoretical approach. Icarus, 360, 114318.

Crotwell, H. P., Owens, T. J., & Ritsema, J. (1999). The TauP Toolkit: Flexible seismic travel-time and ray-path utilities. Seismological Research Letters, 70, 154-160.

Crow-Willard, E. N., & Pappalardo, R. T. (2015). Structural mapping of Enceladus and implications for formation of tectonized regions. Journal of Geophysical Research: Planets, 120(5), 928-950.

Das, I., Padman, L., Bell, R. E., Fricker, H. A., Tinto, K. J., Hulbe, C. L., ... & Siegfried, M. R. (2020). Multidecadal basal melt rates and structure of the Ross Ice Shelf, Antarctica, using airborne ice penetrating radar. Journal of Geophysical Research: Earth Surface, 125(3), e2019JF005241.

Davies, D., Kelly, E. J., & Filson, J. R. (1971). Vespa process for analysis of seismic signals. Nature Physical Science, 232, 8-13.

Diez, A., Bromirski, P. D., Gerstoft, P., Stephen, R. A., Anthony, R. E., Aster, R. C., ... & Wiens, D. A. (2016). Ice shelf structure derived from dispersion curve analysis of ambient seismic noise, Ross Ice Shelf, Antarctica. Geophysical Journal International, 205(2), 785-795.

Dziewonski, A. M., & Anderson, D. L. (1981). Preliminary reference Earth model. Physics of the Earth and Planetary Interiors, 25(4), 297-356.

Figueredo, P. H., Greeley, R., Neuer, S., Irwin, L., & Schulze-Makuch, D. (2003). Locating potential biosignatures on Europa from surface geology observations. Astrobiology, 3(4), 851-861.

Fuchs, K., & Müller, G. (1971). Computation of synthetic seismograms with the reflectivity method and comparison with observations. Geophysical Journal International, 23(4), 417-433.

Goldstein, P., Dodge, D., Firpo, M., Minner, L., Lee, W. H. K., Kanamori, H., ... & Kisslinger, C. (2003). SAC2000: Signal processing and analysis tools for seismologists and engineers. The IASPEI international handbook of earthquake and engineering seismology, 81, 1613-1620.

Goodling, P. J., Lekic, V., & Prestegaard, K. (2018). Seismic signature of turbulence during the 2017 Oroville Dam spillway erosion crisis. Earth Surface Dynamics, 6(2), 351-367.

Grebmeier, J. M. (2022). Applying understanding of Earth systems, including climate change, to exploration of other ocean worlds. Oceanography, 35(1), 45–53.

Hand, K. P., Chyba, C. F., Priscu, J. C., Carlson, R. W., & Nealson, K. H. (2009). Astrobiology and the potential for life on Europa. Europa, 589-629.

Haran, T., Klinger, M., Bohlander, J., Fahnestock, M., Painter, T., & Scambos, T. (2018). MEaSUREs MODIS Mosaic of Antarctica 2013–2014 (MOA2014) Image Map; Version 1. MOA2014 coastline, 1.

Hendrix, A. R., Hurford, T. A., Barge, L. M., Bland, M. T., Bowman, J. S., Brinckerhoff, W., ... & Vance, S. D. (2019). The NASA roadmap to ocean worlds. Astrobiology, 19(1), 1-27.

Hogg, A. E., Gilbert, L., Shepherd, A., Muir, A. S., & McMillan, M. (2021). Extending the record of Antarctic ice shelf thickness change, from 1992 to 2017. Advances in Space Research, 68(2), 724-731.

Huang, M. H., Udell Lopez, K., & Olsen, K. G. (2022). Icequake-Magnitude Scaling Relationship Along a Rift Within the Ross Ice Shelf, Antarctica. Geophysical Research Letters, 49(10), e2022GL097961.

King, E. C., & Bell, A. C. (1996). New seismic data from the Ronne Ice shelf, Antarctica. Geological Society, London, Special Publications, 108(1), 213-226.

Kirchner, J. F., & Bentley, C. R. (1979). Seismic short-refraction studies on the Ross Ice Shelf, Antarctica. Journal of Glaciology, 24(90), 313-319.

Klein, E., Mosbeux, C., Bromirski, P. D., Padman, L., Bock, Y., Springer, S. R., & Fricker, H. A. (2020). Annual cycle in flow of Ross Ice Shelf, Antarctica: contribution of variable basal melting. Journal of Glaciology, 66(259), 861-875.

Lawrence, J. D., Mullen, A. D., Bryson, F. E., Chivers, C. J., Hanna, A. M., Plattner, T., ... & Schmidt, B. E. (2023). Subsurface science and search for life in ocean worlds. The Planetary Science Journal, 4(2), 22.

Lombardi, D., Gorodetskaya, I., Barruol, G., & Camelbeeck, T. (2019). Thermally induced icequakes detected on blue ice areas of the East Antarctic ice sheet. Annals of Glaciology, 60(79), 45-56.

Lorenz, R. D., Turtle, E. P., Barnes, J. W., Trainer, M. G., Adams, D. S., Hibbard, K. E., ... & Bedini, P. D. (2018). Dragonfly: A rotorcraft lander concept for scientific exploration at Titan. Johns Hopkins APL Technical Digest, 34(3), 14.

Marusiak, A. G., Tharimena, S., Panning, M. P., Vance, S. D., Boehm, C., Stähler, S., & Van Driel, M. (2023). Estimating the 3D structure of the Enceladus ice shell from Flexural and Crary waves using seismic simulations. Earth and Planetary Science Letters, 603, 117984.

Marusiak, A. G., Vance, S., Panning, M. P., Běhounková, M., Byrne, P. K., Choblet, G., ... & Wang, S. (2021). Exploration of icy ocean worlds using geophysical approaches. The Planetary Science Journal, 2(4), 150.

Müller, G. (1985). The reflectivity method: a tutorial. Journal of Geophysics, 58(1-3), 153-174.

National Academies of Sciences, Engineering, and Medicine. (2022). Origins, Worlds, and Life: A Decadal Strategy for Planetary Science and Astrobiology 2023-2032. Washington, DC: The National Academies Press. https://doi.org/10.17226/26522.

Olinger, S. D., Lipovsky, B. P., Wiens, D. A., Aster, R. C., Bromirski, P. D., Chen, Z., ... & Stephen, R. A. (2019). Tidal and thermal stresses drive seismicity along a major Ross Ice Shelf rift. Geophysical Research Letters, 46(12), 6644-6652.

Olsen, K. G., Hurford, T. A., Schmerr, N. C., Huang, M. H., Brunt, K. M., Zipparo, S., ... & Aster, R. C. (2021). Projected Seismic Activity at the Tiger Stripe Fractures on Enceladus, Saturn, From an Analog Study of Tidally Modulated Icequakes Within the Ross Ice Shelf, Antarctica. Journal of Geophysical Research: Planets, 126(6), e2021JE006862.

Panning, M. P., Stähler, S. C., Huang, H. H., Vance, S. D., Kedar, S., Tsai, V. C., ... & Lorenz, R. D. (2018). Expected seismicity and the seismic noise environment of Europa. Journal of Geophysical Research: Planets, 123(1), 163-179.

Park, J., Vernon III, F. L., & Lindberg, C. R. (1987). Frequency dependent polarization analysis of high-frequency seismograms. Journal of Geophysical Research: Solid Earth, 92(B12), 12664-12674.

Porco, C., DiNino, D., & Nimmo, F. (2014). How the geysers, tidal stresses, and thermal emission across the south polar terrain of Enceladus are related. The Astronomical Journal, 148(3), 45.

Podolskiy, E. A., & Walter, F. (2016). Cryoseismology. Reviews of geophysics, 54(4), 708-758.

Huang, Q., Schmerr, N. C., King, S. D., Kim, D., Rivoldini, A., Plesa, A. C., ... & Banerdt, W. B. (2022). Seismic detection of a deep mantle discontinuity within Mars by InSight. Proceedings of the National Academy of Sciences, 119(42), e2204474119.

Rhoden, A. R., Hurford, T. A., Spitale, J., Henning, W., Huff, E. M., Bland, M. T., & Sajous, S. (2020). The formation of Enceladus' Tiger Stripe Fractures from eccentricity tides. Earth and Planetary Science Letters, 544, 116389.

Rost, S., & Thomas, C. (2002). Array seismology: Methods and applications. Reviews of geophysics, 40(3), 2-1.

Schulson, E. M., & Fortt, A. L. (2012). Friction of ice on ice. Journal of Geophysical Research: Solid Earth, 117(B12).

Shearer, P. M. (1991). Constraints on upper mantle discontinuities from observations of long-period reflected and converted phases. Journal of Geophysical Research: Solid Earth, 96(B11), 18147-18182.

Souček, O., Běhounková, M., Schroeder, D. M., Wolfenbarger, N. S., Kalousová, K., Steinbrügge, G., & Soderlund, K. M. (2023). Radar attenuation in Enceladus' ice shell: Obstacles and opportunities for constraining shell thickness, chemistry, and thermal structure. Journal of Geophysical Research: Planets, 128, e2022JE007626. https://doi.org/10.1029/2022JE007626

Stähler, S. C., Panning, M. P., Vance, S. D., Lorenz, R. D., van Driel, M., Nissen-Meyer, T., & Kedar, S. (2018). Seismic wave propagation in icy ocean worlds. Journal of Geophysical Research: Planets, 123(1), 206-232.

Stähler, S. C., Khan, A., Banerdt, W. B., Lognonné, P., Giardini, D., Ceylan, S., ... & Smrekar, S. E. (2021). Seismic detection of the martian core. Science, 373(6553), 443-448.

Stevens, C., Hulbe, C., Brewer, M., Stewart, C., Robinson, N., Ohneiser, C., & Jendersie, S. (2020). Ocean mixing and heat transport processes observed under the Ross Ice Shelf control its basal melting. Proceedings of the National Academy of Sciences, 117(29), 16799-16804.

Tinto, K. J., Padman, L., Siddoway, C. S., Springer, S. R., Fricker, H. A., Das, I., ... & Bell, R. E. (2019). Ross Ice Shelf response to climate driven by the tectonic imprint on seafloor bathymetry. Nature Geoscience, 12(6), 441-449.

Trnkoczy, A. (2009). Understanding and parameter setting of STA/LTA trigger algorithm. In New Manual of Seismological Observatory Practice (NMSOP) (pp. 1-20). Deutsches GeoForschungsZentrum GFZ.

Vance, S. D., Kedar, S., Panning, M. P., Stähler, S. C., Bills, B. G., Lorenz, R. D., ... & Rhoden, A. R. (2018). Vital signs: seismology of icy ocean worlds. Astrobiology, 18(1), 37-53.

Vance, S. D., Journaux, B., Hesse, M., & Steinbrügge, G. (2021). The salty secrets of icy ocean worlds. Journal of Geophysical Research: Planets, 126(1), e2020JE006736.

Walker, C. C., Bassis, J. N., Fricker, H. A., & Czerwinski, R. J. (2013). Structural and environmental controls on Antarctic ice shelf rift propagation inferred from satellite monitoring. Journal of Geophysical Research: Earth Surface, 118(4), 2354-2364.

Watkins, R. H., Bassis, J. N., & Thouless, M. D. (2021). Roughness of ice shelves is correlated with basal melt rates. Geophysical Research Letters, 48(21), e2021GL094743.

Wiens, D., Aster, R., & Bromirski, P. (2014). Collaborative Research: Collaborative Research: Dynamic Response of the Ross Ice Shelf to Ocean Waves and Structure and Dynamics of the Ross Sea from a Passive Seismic Deployment on the Ross Ice Shelf [Data set]. International Federation of Digital Seismograph Networks. https://doi.org/10.7914/SN/XH_2014

Wolfenbarger, N. S., Buffo, J. J., Soderlund, K. M., & Blankenship, D. D. (2022). Ice shell structure and composition of ocean worlds: Insights from accreted ice on Earth. Astrobiology, 22(8), 937-961.

Zhan, Z., Tsai, V. C., & Clayton, R. W. (2013). Spurious velocity changes caused by temporal variations in ambient noise frequency content. Geophysical Journal International, 194(3), 1574-1581.

Appendix

I. Stacking Python Code

```
import glob,os,math
import numpy as np
from obspy import read
import matplotlib.pyplot as plt
import pandas as pd
import scipy
from sigfig import round


# Switch to directory with SAC files with SNR in headers are in
os.chdir('/Users/siobh/Documents/SACFiles/Seismic_Data_Files/sacfiles_withqual_labels_updated/')


# List of all *.sac files
file_list = []
for file_name in glob.glob('/Users/siobh/Documents/SACFiles/Seismic_Data_Files/sacfiles_withqual_labels_updated/*HHZ.sac'):
    file_list.append(file_name)


# Reading in headers of all SAC files
st = read('*HHZ.sac',format='SAC',headonly=True)


# Makes of list of files with both a p-wave and a Rayleigh wave pick
events = []
for i in range(len(st)):
    if "a" in st[i].stats.sac:
```

```
        if "t0" in st[i].stats.sac:
            events.append(file_list[i])

# Finding Rayleigh-pwave Times
diff = []
theirsnr = [] # For seeing SNR stats
for i in range(len(events)):
    newstream = read(events[i],format='SAC')
    p = newstream[0].stats.sac.a
    r = newstream[0].stats.sac.t0 # Adding Rayleigh wave pick
    dq = r-p # Difference of Rayleigh-Pwave time
    diff.append(dq)
    snr = newstream[0].stats.sac.user0
    theirsnr.append(snr)

# Sorting out events whose SNR is below cut-off
newdiff = []
modevents = []
newsnrlist = []
for i in range(len(theirsnr)):
    thesnr = theirsnr[i]
    if thesnr >= np.percentile(theirsnr,10): # Line to adjust min to cut-off SNR
        newdiff.append(diff[i])
        modevents.append(events[i])
        newsnrlist.append(theirsnr[i])


#### Parameters to Adjust #####
```

```
binnumber = 20 # Adjust as wanted
upperrange = np.max(newdiff) # Upper value to form bins with
# NOTE: This upper range will change with changing min SNR cuttoff
# The bins will calculate based on the maximum difference after cutting off for SNR

# Forming the width of bins
binwidth1 = float(upperrange)/binnumber
binwidth = round(binwidth1,2)

# Sorting events into bins
#hist = np.histogram(newdiff,bins=binnumber,range=(0,upperrange)) # Adjust range as wanted
#edge = hist[:][1]
cat = pd.cut(newdiff,bins=binnumber,right=False) # Forms histogram categories based on parameters
bins = cat.categories
lab1 = [str(pd.Interval(np.round(i.left,decimals=2),np.round(i.right,decimals=2),closed='left')) for i in bins]

# Dictionary containing which files are in which histogram category
values = {}
for i in bins:
    values[str(i)] = []
for i in range(len(newdiff)):
    value = newdiff[i]
    for j in range(len(bins)):
        logic = value in bins[j]
        if logic==True:
            correspond = modevents[i]
```

```
            values[str(bins[j])].append(correspond)

# Number of events in each bin
binnumberevents = []
for i in values.values():
    lengthbin = len(i)
    binnumberevents.append(lengthbin)

# Labels combining the time difference and number of events in each bin
finallabels = []
for i,j in zip(lab1,binnumberevents):
    finlab = i+", "+str(j)+" events"
    finallabels.append(finlab)

# Variables for helping for plotting
distances = np.arange(0,binnumber*2,2.0) # Used for spacing lines on combined stacked plot
potential_colors =
['k','m','b','g','r','c','orange','brown','purple','olive','lime','dodgerblue','teal','indigo','mediumvioletred','tan','goldenrod','lightseagreen','pink','thistle','orangered','chocolate','darkkhaki','darkolivegreen','seagreen'] # Colors for plot
thekeys = list(values.keys()) # Categories

# Function to round down given value to nearest value of a type of multiple
def round_down(x, a):
    return np.floor(x / a) * a

def round_decimals_down(number:float, decimals:int=2):
    """
    Returns a value rounded down to a specific number of decimal places.
```

```
    """
    if not isinstance(decimals, int):
        raise TypeError("decimal places must be an integer")
    elif decimals < 0:
        raise ValueError("decimal places has to be 0 or more")
    elif decimals == 0:
        return math.floor(number)

    factor = 10 ** decimals
    return math.floor(number * factor) / factor

"""
# Overlap Stacking Plot
plt.figure(figsize=(12.5,10)) # May wish to adjust
count = -1
for i in values.values():
    count += 1
    try: # Handles if blank bin
        first = read(i[0],format='SAC')
        for j in i[1:]:
            first += read(j,format='SAC')
        first.normalize(global_max=True)
        for k in first:
            #update = k.times() - (k.stats.sac.a-k.stats.sac.b) # Adjust to changing to based on
Rayleigh wave arrival
            update = k.times() - (k.stats.sac.a-k.stats.sac.b)
            plt.plot(update,k.data+distances[count],c=potential_colors[count],linewidth=0.5)
    except IndexError:
        pass
```

```
plt.xlabel('Time since P-Wave Arrival') # Adjust depending on type of wave aligning by
plt.ylabel('Normalized Amplitude')
plt.title('Binned by %s Seconds, Same P-Wave Arrival' %str(binwidth)) # Adjust depending on bin size, type of wave arriving
plt.axvline(x=0,linestyle='--')
plt.legend((values.keys()))


# Individual overlapping stacking figures
count = -1
for i in values.values():
    count += 1
    plt.figure(figsize=(8,6))
    try: # Handles if blank bin
        first = read(i[0],format='SAC')
        for j in i[1:]:
            first += read(j,format='SAC')
        #first.normalize(global_max=True)
        for k in first:
            #update = k.times() - (k.stats.sac.a-k.stats.sac.b) # Adjust to changing to based on Rayleigh wave arrival
            update = k.times() - (k.stats.sac.a-k.stats.sac.b)
            k.data = 2*((k.data - np.min(k.data))/(np.max(k.data) - np.min(k.data))) - 1
            k.detrend('demean')
            plt.plot(update,k.data+distances[count],c=potential_colors[count],linewidth=0.5)
    except IndexError:
        pass
    numberofeventsinplot = len(first)
    plt.xlabel('Time since P-Wave Arrival')
    plt.ylabel('Normalized Amplitude')
```

```
    plt.title('Aligned Seismic Events, Bin Size %s, %s events'
%(thekeys[count],str(numberofeventsinplot))) # Adjust depending on bin size, type of wave
arriving
    plt.axvline(x=0,linestyle='--')



count = -1
for i in values.values():
    count += 1
    plt.figure(figsize=(8,6))
    try: # Handles if blank bin
        first = read(i[0],format='SAC')
        for j in i[1:]:
            first += read(j,format='SAC')
        #first.normalize(global_max=True)
        for k in first:
            #update = k.times() - (k.stats.sac.a-k.stats.sac.b) # Adjust to changing to based on
Rayleigh wave arrival
            update = k.times() - (k.stats.sac.a-k.stats.sac.b)
            plt.plot(update,k.data,c=potential_colors[count],linewidth=0.5)
    except IndexError:
        pass
    numberofeventsinplot = len(first)
    plt.xlabel('Time since P-Wave Arrival')
    plt.ylabel('Normalized Amplitude')
    plt.title('Bin %s, Same P-Wave Arrival, %s events'
%(thekeys[count],str(numberofeventsinplot))) # Adjust depending on bin size, type of wave
arriving
    plt.axvline(x=0,linestyle='--')
```

```
"""
# The stacking loop for summing together traces in the same bin and plotting them on the same plot
plt.figure(figsize=(12.5,10))
count = -1
for i in values.values():
    originaldataset = []
    originaldataset1 = []
    count += 1
    starttimes = []
    endttimes = []
    try:
        if len(i)>1:
            first = read(i[0],format='SAC')
            for j in i[1:]:
                first += read(j,format='SAC')
            first.normalize(global_max=True) # Normalize trace to maximum in stream
            for k in first:
                # Align times by p-wave arrival
                update = k.times() - (k.stats.sac.a-k.stats.sac.b) # Aligns by p-wave arrival, Adjust IF changing to based on Rayleigh wave arrival
                #update = k.times() - (k.stats.sac.t0-k.stats.sac.b)
                starttimes.append(update[0])
                endttimes.append(update[1600])
                if len(update) != 1601 :
                    print("Check time lengths, may be issue")
            minstart = min(starttimes) # Minimum possible start time of traces once aligned
            minstart = float(round_down(minstart,0.005)) # Rounds down possible start time to nearest 0.005 s
```

```
        maxend = max(endttimes) # Maximum possible end time of traces once aligned
        maxend = float(round_down(maxend,0.005)) # Rounds down this maximum time to nearest 0.005 s
        newtimes = np.arange(minstart,maxend+0.001,0.005) # Creates axis of possible times for stack
        blankdata = np.zeros(len(newtimes),)
        for stream in first: # For each component trace in a stack
            update = stream.times() - (stream.stats.sac.a-stream.stats.sac.b) # Aligns by p-wave arrival, Adjust IF changing to based on Rayleigh wave arrival
            update = round_down(update,0.005)
            times = update
            stream.data = 2*((stream.data - np.min(stream.data))/(np.max(stream.data) - np.min(stream.data))) - 1
            stream.detrend('demean')
            newdata = stream.data
            originaldataset1 = np.concatenate((update,newdata))
            originaldataset = np.reshape(originaldataset1,(2,len(newdata)))
            thedatastart = round(float(update[0]),decimals=3)
            thedataend = round(float(update[1600]),decimals=3)
            if thedatastart>minstart:
                timestofill = np.arange(minstart,float(thedatastart-0.001),0.005)
                timestofill1 = len(timestofill)
                empty_values1 = np.zeros(timestofill1,)
                newdata = np.ma.concatenate([empty_values1,newdata])
                times = np.ma.concatenate([timestofill,times])
            if maxend>thedataend:
                timestofill2 = np.arange(float(thedataend+0.005),float(maxend+0.001),0.005)
                timestofill3 = len(timestofill2)
                empty_values2 = np.zeros(timestofill3,)
                newdata = np.ma.concatenate([newdata,empty_values2])
```

```
                times = np.ma.concatenate([times,timestofill2])
            blankdata = np.add(blankdata,newdata)
        themaxamp = np.max(blankdata)
        theminamp = np.min(blankdata)
        normalized_data = []
        for jj in blankdata:
            newvalu = (jj-theminamp)/(themaxamp-theminamp)
            normalized_data.append(newvalu)
        normalized_data = np.array(normalized_data)
        print("Got to this step")
        mode = scipy.stats.mode(normalized_data)
        normalized_data = np.where(normalized_data ==
float(mode[0]),np.nan,normalized_data)

plt.plot(newtimes,normalized_data+distances[count],c=potential_colors[count],linewidth=0.7
5,label=finallabels[count])
    elif len(i)==1:
        first = read(i[0],format='SAC')
        update = first[0].times() - (first[0].stats.sac.t0-first[0].stats.sac.b)
        first[0].data = 2*((first[0].data - np.min(first[0].data))/(np.max(first[0].data) -
np.min(first[0].data))) - 1
        first[0].detrend('demean')
        newdata = first[0].data
        themaxamp = np.max(newdata)
        theminamp = np.min(newdata)
        normalized_data = []
        for jj in newdata:
            newvalu = (jj-theminamp)/(themaxamp-theminamp)
            normalized_data.append(newvalu)
        normalized_data = np.array(normalized_data)
```

```
            print("Got to elif step")

    plt.plot(update,normalized_data+distances[count],c=potential_colors[count],linewidth=0.75,label=finallabels[count])
        except IndexError:
            print("Code is not working")
            pass
    plt.xlabel('Time since P-Wave Arrival',fontsize=20) # Adjust depending on type of wave aligning by
    plt.ylabel('Normalized Amplitude',fontsize=20)
    plt.axvline(x=(0),color='k',linewidth=0.5,linestyle='--')
    #plt.title('%s Seconds Binned Summed Stacks' %str(binwidth),fontsize=20) # Adjust depending on bin size, type of wave arriving
    plt.legend(loc=2,fontsize=12,bbox_to_anchor=(1,0.85))
    plt.savefig("bin_%s_summedstack_aligned_pwave.png" %str(binwidth),dpi=300,bbox_inches="tight")
```

II. Event Distance Mapping Code

```
# Code to plot events on map
import os
import matplotlib.pyplot as plt
import numpy as np
import pandas as pd
from mpl_toolkits.basemap import Basemap
import glob
import math
import geopy
from geopy.distance import geodesic
import obspy
from obspy import read
```

```
# Define function to find nearest value
def find_nearest(array, value):
    array = np.asarray(array)
    idx = (np.abs(array - value)).argmin()
    return array[idx]



# Locate using previously calculated back_az and time between arrivals for distance
#%% Read in files, get ready to plot
station = 'DR14'


file_list = []
for file_name in
glob.glob('/Users/siobh/Documents/SACFiles/Seismic_Data_Files/sacfiles_withqual_labels_upd
ated/*HHZ.sac'):
    file_list.append(file_name)


# Reading in all SAC files
os.chdir('/Users/siobh/Documents/SACFiles/Seismic_Data_Files/sacfiles_withqual_labels_updat
ed')
st = read('*HHZ.sac',format='SAC',headonly=True)


events = []
events2 = []
differences = []
theirsnr = [] # For seeing SNR stats
for i in range(len(st)):
    if "a" in st[i].stats.sac:
        if "t0" in st[i].stats.sac:
```

```
        events.append(file_list[i])
        diff = st[i].stats.sac.t0-st[i].stats.sac.a
        differences.append(diff)
        eventname =
file_list[i].replace('/Users/siobh/Documents/SACFiles/Seismic_Data_Files/sacfiles_withqual_labels_updated\\','')
        eventname = int(eventname.replace("_XH.DR14..HHZ.sac",""))
        events2.append(eventname)
        snr = st[i].stats.sac.user0
        theirsnr.append(snr)


# Filtering out less certain events
# Sorting out events whose SNR is below cut-off
newdiff = []
modevents = []
modevents2 = []
newsnrlist = []
for i in range(len(theirsnr)):
    thesnr = theirsnr[i]
    if thesnr >= np.percentile(theirsnr,10): # Line to adjust min to cut-off SNR
        newdiff.append(differences[i])
        modevents.append(events[i])
        modevents2.append(events2[i])
        newsnrlist.append(theirsnr[i])


events = modevents
events2 = modevents2
theirsnr = newsnrlist
differences = newdiff
```

```
azlocation =
'C:\\Users\\siobh\\Documents\\SACFiles\\Full_Data\\8s_event_windows/azimuthvaluemasterlist.
txt'
with open(azlocation,'r') as listaz:
    lines = [line.rstrip('\n').split() for line in listaz]


potentialazevents = [part[0] for part in lines]
theaz = [part[1] for part in lines]


summaryofdistanceinfo = []
possibleevents = []
for i in events2:
    try:
        where = potentialazevents.index(str(i))
        azmaster = theaz[where]
        where2 = events2.index(i)
        difmaster = differences[where2]
        summaryofdistanceinfo.append((azmaster,difmaster))
        possibleevents.append(i)
    except:
        print("Missing az for "+str(i))
#%% Calculate and write out distance and resulting lat/lon of each event
# This plots in WGS-84


#vel_p = 3.77 # 3.77 km/s from Diez et al., 2016 - 10/9/2020
vel_p = 3.80 # Revised value based on previous studies, see vp_estimate spreadsheet
vel_R = 1.55 # 1.55km/s from Olinger et al., 2019 - 10/9/2020 Use this value in paper
```

```
# For calculating error
p_pick = 0.084 # Manual pick window error on p-wave pick
r_pick = 0.105 # Manual pick window error on rayeligh wave pick, likely use since highest of differences
#res = 0.005 # Resolution limit of picks
vr = 0.05 # Error on rayleigh wave velocity, based on olinger 2019
vp = 0.05 # Error based on range of estimates of Vp

dv_error = np.sqrt((vp/(vel_p**2))**(2)+(vr/(vel_R**2))**(2))
dt_error = np.sqrt(p_pick**(2)+r_pick**(2))

locations = []
#dr14_lat = -79.142601
#dr14_lon = 179.947601
if station == 'DR15':
    st_lat = -79.492798 #DR15
    st_lon = -179.919296 #DR15
elif station == 'DR14':
    st_lat = -79.142601
    st_lon = 179.947601
else:
    print('Need station coordinates!')

for el in range(len(summaryofdistanceinfo)):
    try:
        az = float(summaryofdistanceinfo[el][0])

        dt = float(summaryofdistanceinfo[el][1])
```

```
        dv = 1/vel_R - 1/vel_p

        dist = dt / dv # in km. Formula is: dist = (ts - tp)/(1/Vs - 1/Vp).
        dist_error = (np.sqrt(((dt**2)*dv_error**2)+((dt_error**2)*dv**2)))/(dv**2)

        origin = geopy.Point(st_lat, st_lon)
        destination = geodesic(kilometers = dist).destination(origin, az)

        ev_lat = destination.latitude
        ev_lon = destination.longitude


        locations.append([station, possibleevents[el], dist, az, ev_lat, ev_lon, dt, dist_error])
    except:
        print("Error for event "+str(possibleevents[el]))
locations_df = pd.DataFrame(locations, columns = ['station','event','dist','az','ev_lat','ev_lon',
'delta_t','dist_error'])

az_list = [el[3] for el in locations]
dist_list = [el[2] for el in locations]
dt_list = [el[6] for el in locations]
#%% Map of full station area
plt.figure(figsize = (6,6))
# Tight zoom in
llcrnrlon2=179.1
llcrnrlat2=-79.2
urcrnrlon2=-179.6
urcrnrlat2=-79.05
import rasterio
```

```
from rasterio.windows import Window
import pyproj
test1 = 'C:/Users/siobh/Downloads/moa125_2014_hp1_v02.tif'
p = pyproj.Proj(init="epsg:%s" % 3031, preserve_units=True)
xmin,ymin = p(llcrnrlon2,llcrnrlat2)
xmax,ymax = p(urcrnrlon2,urcrnrlat2)

projectionextents = (xmin,xmax,ymin,ymax)
img = rasterio.open(test1)
x1,y1 = img.index(xmin,ymax)
x0,y0 = img.index(xmax,ymin)
image = img.read(1,window=Window.from_slices((x0,x1), (y0,y1)))

fig = plt.figure(figsize=(8,8))

map = Basemap(epsg = 3031, # epsg: 3031 is Antarctic Stereographic, wgs-84: 4326
            resolution = 'i',  llcrnrlon=urcrnrlon2, #'f' option gives full resolution
            llcrnrlat=llcrnrlat2, urcrnrlon=llcrnrlon2, urcrnrlat=urcrnrlat2)
map.drawmeridians(np.arange(0,360,0.5), labels=[0,1,0,1],fontsize=12)
map.drawparallels(np.arange(-90,90,0.05), labels=[1,0,0,0],fontsize=12)

map.drawmapscale(-179.89,-79.059,179.12,-
79.19,10,barstyle='fancy',fontsize=12,labelstyle='simple',yoffset=0.005)
for i in range(1):
   lon = st_lon
   lat = st_lat
   if lat >= llcrnrlat2 and lat <= urcrnrlat2: #only plot if event is within geographic range of this
figure
      x,y = map(lon,lat)
```

```
        color = 'red'
#           color = 'blue'
        map.plot(x,y, marker = '^', markersize = 10, mew=1, c = color)   #marker = (numsides, style, angle), mew = thickness of outline



# Plot events
for j in range(len(locations)):
    ev_lat = locations[j][4]
    ev_lon = locations[j][5]
    x1,y1 = map(ev_lon,ev_lat)
    map.plot(x1,y1, marker = '.', markersize = 10, mew=1, c = 'b')


map.imshow(image,extent=projectionextents,alpha=1,cmap='binary')
plt.tight_layout()
fig.savefig('map_of_distances.png',dpi=500)
```

III. Honor Code

I pledge on my honor that I have not given or received any unauthorized assistance or plagiarized on this assignment.